

Microfluidic Viscometer for Tear Films and Other Biofluids

by

Wasim Kapadia

A thesis

presented to the University of Waterloo

in fulfillment of the

thesis requirement for the degree of

Master of Applied Science

in

Mechanical and Mechatronics Engineering

Waterloo, Ontario, Canada, 2022

© Wasim Kapadia 2022

Author's Declaration

I hereby declare that I am the sole author of this thesis. This is a true copy of the thesis, including any required final revisions, as accepted by my examiners.

I understand that my thesis may be made electronically available to the public.

Abstract

A microfluidic viscometer platform is developed and validated for measuring microliter-volume liquid samples, such as human tear films. The microfluidic viscometer combines an optically clear acrylic chip with a hydrophobic surface coating together with a syringe pump to control the sample flow rate. Additional functionally supporting devices, including a camera and a differential pressure transducer, were used for analysis. It has been demonstrated that the microfluidic viscometer could measure the viscosities of both Newtonian and non-Newtonian liquid samples, and their relevant calculations are presented. The microfluidic viscometer has potential applications in measuring the rheological properties of biofluids for diagnostic applications.

Acknowledgements

I would like to thank my supervisor Professor Carolyn Ren for her patience and educational support in every step of this work. I would also like to thank Dr. Sean Peterson and Dr. Chau-Minh Phan, my thesis committee, for guidance.

The help and guidance of Dr. Ning Qin and Dr. Pei Zhao has been invaluable throughout this work. In addition, I would like to thank Dr. Lyndon Jones and Dr. Lacey Haines for their suggestions and perspective.

Table of Contents

Author’s Declaration	ii
Abstract	iii
Acknowledgements	iv
List of Figures	viii
List of Tables.....	x
Chapter 1 Introduction.....	1
Chapter 2 Literature Review	3
2.1 Background	3
2.1.1 Dry Eye Disease	3
2.1.2 Tear Film Viscosity as a Potential Diagnostic Measurement for DED	4
2.1.3 Challenges (shear rate and volume).....	5
2.2 Existing Rheometric Measuring Technologies.....	5
2.2.1 Rotational Viscometer	6
2.2.2 Capillary Viscometer.....	7
2.2.3 Falling Ball Viscometer.....	8
2.2.4 Summary	8
2.3 Microfluidic Viscometers.....	8
2.3.1 Pressure Sensing Microfluidic Viscometers.....	9
2.3.2 Surface Tension Microfluidic Viscometers	9
2.3.3 Summary	10
2.4 Research Objective.....	10
2.4.1 Research Aims.....	10
2.4.2 Project Objectives.....	11

Chapter 3 Methodology	12
3.1 Rheology Measurement Method	12
3.1.1 Design Principle	12
3.2 Materials and Fabrication	13
3.2.1 Microfluidic Chip	13
3.2.2 Manifold	17
3.3 Characterization.....	18
3.3.1 Pump.....	18
3.3.2 Differential Pressure Transducer	18
3.3.3 Video Camera.....	20
Chapter 4 Shear-Thinning and Temperature-Dependent Viscosity Relationships of Commercially Available Eye Drops [4].....	22
4.1 Ocular Lubricants	22
4.2 Materials and Methods	24
4.3 Results	26
4.3.1 Ostwald de Wale relationship: Mathematical model.....	28
4.4 Discussion	32
Chapter 5 Development of the System.....	33
5.1 Idea (equation).....	33
5.1.1 Theory	33
5.2 Method.....	35
5.3 Testing Methodology.....	36
5.4 Setup and Running a Test.....	36
5.5 Validation	38

5.6 Discussion	45
Chapter 6 Further Validation and Testing	51
6.1 Saliva	51
6.2 Blood	53
Chapter 7 Summary	56
Chapter 8 Future Recommendations	57
References	58
Appendices	62
Appendix A	62
Appendix B.....	65
Appendix C.....	66

List of Figures

Figure 1. Microfluidic viscometer overview	11
Figure 2. Schematic of the proposed microfluidic viscometer.	13
Figure 3. Microfluidic chip: (a) four laser cut layers of the microfluidic chip; (b) assembled microfluidic chip	14
Figure 4. Main components of the microfluidic chip	15
Figure 5. 3D printed manifold: (a) cover; and (b) base	18
Figure 6. Pressure-Voltage Scaling Parameters: (a) Relationship found using flow controller; and (b) NI-DAQmx inputs	19
Figure 7. Differential pressure transducer pinout	20
Figure 8. The shear viscosity measurement setup: (a) the rheometer; (b) a refrigerated bath circulator (model: mx 71 r-20, VWR International); and (c) a warming bath circulator (left; model: SC150-S45, Thermo Fisher Scientific) connected to the rheometer.	25
Figure 9. Shear viscosities of 12 different commercial eye drops at (a) $24.6 \pm 1.2^\circ\text{C}$, (b) $34.5 \pm 0.1^\circ\text{C}$, and (c) $4.3 \pm 0.3^\circ\text{C}$. Refresh Optive Gel Drops (<i>heavy cross</i>), Systane Ultra Hydration (<i>rhombus</i>), Refresh Optive Fusion (square), Blink Moisturizing Lubricant Eye drops (<i>X</i>), Bio True (<i>pentagon</i>), Long Lasting Relief (<i>circle</i>), Hylo Comod (<i>starburst</i>), Refresh Optive Advanced (<i>diamond</i>), Systane Complete (<i>triangle</i>), Systane Ultra High Performance (<i>star</i>), Thealoz Duo (<i>hexagon</i>), Systane Balance Lipid Layer Formula (<i>circled X</i>)	27
Figure 10. The power-law fitting (dashed line) of the shear viscosity data of Systane Ultra Hydration (solid line) at room temperature, where K and n are $49.64 \text{ mPa}\cdot\text{s}^{0.893}$ and 0.893, respectively.....	28
Figure 11. 2D representation of the sample plug moving through a section of the microfluidic channel	35
Figure 12. The microfluidic viscometer setup: (a) diagram with (11) syringe pump, (12) DC power supply, (13) differential pressure transducer, (14) video camera, (15) computer with DAQ card, (40) manifold with microfluidic chip; (b) picture.	37
Figure 13. Viscosity of different weight percent glycerol in water solutions measured by the commercial rheometer (black) and the microfluidic viscometer (orange) ($n=3$).....	40
Figure 14. Glycerol plug moving through the microchannel from left to right at (a) $t = 20.8 \text{ s}$, and (b) $t = 21.8 \text{ s}$	40

Figure 15. Plot of the natural logarithm of the shear stress versus the natural logarithm of shear rate for Systane Ultra High Performance (Alcon Laboratories, Inc.) eye drops	41
Figure 16. Systane Ultra High Performance (Alcon Laboratories, Inc.) eye drops measured using the commercial rheometer (blue) and the microfluidic viscometer (orange).	42
Figure 17. Viscosity of normal tears (grey) and dry eye tears (red) at two different shear rates	44
Figure 18. The shear viscosity of human tears: (a) measured using Brookfield cone/plate rheometer (blue) and microfluidic viscometer (orange); and (b) shear viscosity taken from Gittings <i>et al.</i> with the orange section of the curve at measured at the same shear rates as the microfluidic viscometer and the grey section of curve measured at same shear rates as measured with the Brookfield cone/plate rheometer.....	52
Figure 19. Hydrogen peroxide treatment validation: (a) contact angle test processed using ImageJ; and (b) section of microchannel before and after flowing porcine blood through and treating it with 0.5% H ₂ O ₂ and water.....	54
Figure 20. Viscosity of porcine whole blood measured using microfluidic viscometer (black circles), average viscosity measured using the microfluidic viscometer (blue line), and expected viscosity based on Rosentrater <i>et al.</i> [67] (orange line)	55

List of Tables

Table 1. Tear Film Properties.....	4
Table 2. Dimensions of the Main Features of the Microfluidic Chip.....	15
Table 3. Ostwald-de Waele coefficients for 12 commercial eye drops.....	30
Table 4. Eye Drop Viscosity Validation.....	43
Table 5. Measurement Uncertainties Using Microfluidic Viscometer.....	47
Table 6. Systematic and Operational Uncertainty Analysis.....	50

Chapter 1

Introduction

Dry eye disease, generally believed to be the result of a combination of excessive tear evaporation and insufficient tear production [1]–[4], affects millions of people worldwide [5]. Work and lifestyle changes, which increasingly rely on display terminals, such as mobile phones and computers, have led to an increased prevalence of the disease [6]. A poor quality tear film can lead to damage to the underlying epithelial cells [7], causing further tear film instability and inflammation [8], exacerbating the disease in a persisting cycle [4], [7], [9], [10].

It is believed that tear film viscosity can be a marker for dry eye disease; however, current commercially available rheometers do not have the capability of measuring the viscosity of samples with volumes on the order of the resting tear film volume. Because of this, a microfluidic viscometer is developed and validated using Newtonian liquids and artificial tears.

The present work describes an apparatus and a method for measuring the viscosity of small volumes of fluid. A dyed sample is introduced into the loading channel of a microfluidic chip that is later housed within a manifold. The manifold is connected via rigid tubing to a syringe that is installed on a syringe pump. As the pump runs, it creates a pressure differential upstream of the sample. The compressed air upstream of the sample provides a driving force to propel the sample to move forward through the microchannel. As the sample moves through, it is visualized, and its movement is captured by a camera positioned above the manifold, which was fabricated with a viewing window. The captured video is then analyzed to obtain the sample velocity, and this parameter, along with the known channel dimension, informs about the on-chip volumetric flow rate. The volumetric flow rate of the sample, microchannel dimension, sample length, capillary pressure, and the differential pressure across the sample length can be used to calculate the sample's viscosity based on the Hagen-Poiseuille equation with the Weissenberg-Rabinowitsch-Mooney correction.

Firstly, in Chapter 2, the relevant background is presented by reviewing existing commercial and microfluidic viscometer systems and methods to illustrate their shortcomings and provide motivation for developing the proposed microfluidic viscometer. Chapter 3 introduces the methodology of the proposed microfluidic viscometer and discusses its key components. Chapter 4 provides an understanding of how to work with artificial tears, and the factors that influence their viscosity, by investigating the shear rate and temperature dependent viscosity relationships of a dozen

commercially available artificial tears. Chapter 5 presents the proposed microfluidic viscometer theory, setup, and validation using glycerol/water and an artificial tear. Chapter 6 provides further validation and testing using blood and saliva. Finally, chapters 7 and 8 present a summary and list future recommendations.

Chapter 2

Literature Review

2.1 Background

2.1.1 Dry Eye Disease

Dry eye disease (DED), which affects an estimated 25 to 30 million individuals globally [11], is a multifactorial disorder that results in an overall degradation of a patient's visual performance [4], [12]. It is a disorder affecting the tear film with a range of possible causes and is characterized by several symptoms [13], namely ocular discomfort, photophobia (light sensitivity), irritation and burning [4], [9], [14].

There are four main etiology-related sub-classifications of DED as outlined by Mark *et. al.*: (1) aqueous deficiency, (2) Meibomian Gland Dysfunction (MGD), (3) goblet cell/ mucin deficiency, and (4) exposure-related DED [13]. The lacrimal gland is responsible for secreting the aqueous component of tears, which contains a number of proteins and electrolytes responsible for maintaining ocular surface health [13]. A reduction in these lacrimal gland secretions, known as aqueous deficiency, accounts for only a tenth of DED cases and is recognized as a volumetric condition [13], [15]. This is usually caused by scarring or blockage of the lacrimal gland [13]. MGD, the second subclassification of DED, also called evaporative dry eye, occurs in over 85% of all cases [15]. The Meibomian glands secrete a thin oily layer that sits on top of the aqueous component of the tear film, which reduces tear evaporation. Uneven distribution of the Meibum over the tear film or a reduction in its quality results in evaporation of tears and exposes the ocular surface to desiccating stress [13]. Goblet cells and mucin interact with the aqueous component of tear films, and their deficiency affects tear film surface tension and stability [13]. Finally, excessive drying of tears due to anatomic defects is the final subclassification of DED. This is usually caused by a mal-positioning of the eyelids or a failure to fully close, exposing the cornea to environmental conditions for an extended period of time, leading to excessive drying [13].

People suffering from DED have consistently identified problems with performing day-to-day tasks that require sustained visual attention like reading, driving and computer use [12], [13]. In addition, this disease is often accompanied by an associated treatment cost [13]. Undiagnosed and untreated DED can cause further exacerbations of the underlying conditions, like a reduction of

corneal sensitivity, which affects patient quality of life [13]. Therefore, early detection and use of ocular lubricants are crucial.

2.1.2 Tear Film Viscosity as a Potential Diagnostic Measurement for DED

Human tears are a complex biological colloid system [16]. Ideally, a healthy tear film retains a uniform thickness (~3 to 10 μm) between blinks, which is necessary for clear visual perception and corneal health [16]. Tears have multiple functions: to provide lubrication between the eye and eyelid, to clear away foreign particulates, and to sustain the corneal and conjunctival epithelial cells [16].

The tear film is composed of three parts: the inner mucin layer (made of soluble mucin macromolecules produced by conjunctival epithelial and goblet cells); the middle aqueous layer (that provides hydration and lubrication to the eye and is created by the lacrimal glands), and the outer lipid layer (that decreases tear evaporation, and is secreted by Meibomian glands) [1], [17]. Table 1 outlines some key properties of tear films. The aqueous component of the tear makes up roughly 90% of its thickness [16]. It contains approximately 0.9 – 1.0 wt% inorganic salts and various proteins (enzymes, immunoglobulins and glycoproteins) [16]. The tear lipids make up the external layer of the tear film and exist as multi-layer films with an aggregate thickness between 30 and 100 nm [16]. The outer lipid layer contains polar and non-polar lipids produced by the Meibomian glands [16]. It preserves ocular surface equilibrium after blinking by promoting the re-spreading, slowing down aqueous-layer evaporation, and providing some anti-microbial activity [16]. The tear film is, therefore, vital to the eye’s health, and any alterations in its “composition, distribution or clearance” can cause dry eye disease [1].

Table 1. Tear Film Properties

Property	Value	Reference
Tear Film Viscosity (DED, low shear)	9 mPa·s	[17]
Tear Film Viscosity (DED, high shear)	1.5 mPa·s	[17]
Tear Film Viscosity (Normal, low shear)	5 mPa·s	[17]
Tear Film Viscosity (Normal, high shear)	1.5 mPa·s	[17]

Tear Film Fluid Type	Shear thinning	
Blink Shear Rate	4,250 – 28,500 /sec	[17]

Tears from dry eyes differ substantially from healthy tears in that they provide a lack of stability. The outer lipid layer’s interfacial elasticity and viscosity are essential contributors to tear stability [16]. Hyperosmolarity is another marker for dry eye disease. This is caused by a reduction in the aqueous volume of the tear film by lacrimal gland deficiencies or by tear film evaporation [13]. However, it is evident from the above table that viscosity can be one metric that optometrists can use to determine if a patient is diagnosed with DED. In addition, one study found that the effective extensional viscosity of dry eye tears was statistically significantly less than healthy tears [18]; however, this study did not look at the shear-rate dependence on the measured viscosity of tears. The authors concluded that viscosity could be a novel parameter to identify and stratify DED and its severity.

2.1.3 Challenges (shear rate and volume)

The issue is that the resting tear film volume in a person’s eye ranges from 3.4 to 10.7 μL [19]. This means it is not possible to measure the viscosity using conventional rheometric methods, which often require working volumes in excess of 500 μL . Furthermore, on the low end, an eye tremor produces shear rates of 0.03 – 0.14 s^{-1} ; on the high end, a blink can result in estimated shear rates of 4250 – 28500 s^{-1} [4], [17]. These are physiologically relevant shear rates that tear films and artificial tears are generally subject to. This means that any method used to ascertain a link between the viscosity of tear films and dry eye disease should be capable of handling very small amounts of sample (under ten microliters) and be capable of measuring the shear viscosity over a wide range of physiologically relevant shear rates. This can be useful for clinicians and researchers looking to discern the physiopathology of dry eye disease and to develop novel, patient-specific contact lenses and artificial tear solutions.

2.2 Existing Rheometric Measuring Technologies

Viscosity is a key physical property of a fluid that provides a quantitative measure of the resistance to its flow. It is defined as the ratio of a fluid’s shear stress to its shear rate and is related to the internal frictional forces of a fluid’s constituent molecules as they move past each other during

fluid flow. Viscosity plays an essential role in helping to understand and predict the behavior of fluids used in everyday life and is useful for appropriately designing industrial process controls. Viscosity is an important parameter of particular interest to scientists and engineers working with oil/lubricants, cosmetics, food and beverages, cannabis oils, batteries, and many other biological fluids.

Various methods have been created to measure the viscosity of liquids, yet choosing an appropriate one, as described in U.S. Pat. No. 6,898,963 B2 (Irani) is contingent on the test conditions (e.g., the temperature at which the measurement will be made and the fluid volume available for the test) and relevant knowledge of the approximate viscosity of the fluid. The three categories of commercial viscometers are the rotational viscometer, capillary viscometer, and falling ball viscometer [20].

2.2.1 Rotational Viscometer

Rotational rheometers are a broad classification that includes coaxial cylinder, cone/plate and parallel-plate rheometers [21]. They are designed to produce conditions that lead to a laminar flow of the sample, which allows for the mathematical treatment of the measured data to produce shear stress, shear rate and viscosity [21]. Rotational rheometers that can measure dynamic viscosity come in two variations. The first requires a controlled-stress input and outputs resulting shear rate. These are known as “CS-rheometers”. The second type requires a controlled shear rate input and outputs the resulting shear stress. These are known as “CR-rheometers”. Furthermore, modern rheometers have two additional design differences in their measurement systems: (1) Searle, in which the rotor rotates, the outer cylinder and lower plates are stationary, and the torque is measured on the axis of rotation; and (2) Couette, in which the outer cylinder or lower plate undergoes rotation and the torque is measured on the non-rotating cone/cylinder [21]. The former has difficulty measuring low viscosity liquids at high shear rates, which may cause turbulent flow of the sample [21], [22]. This means that for a CS-rheometer with a Searle measuring system, a viscosity measurement involves inputting a torque value, measuring the rotor speed and evaluating them to obtain a shear stress and shear rate value, resulting in a corresponding viscosity value [21]. Conversely, a CR-rheometer with a Searle measurement system has an inner cylinder driven by a motor programmed by the user, while the cup is stationary. The resistance of the sheared liquid between the stationary and rotating elements results in a viscosity-related torque, which is detected by a spring [21]. Finally, a CR-rheometer with a Couette measuring system has an outer cylinder that is driven by a motor at a given RPM, which

forces the liquid sample into the annular gap and confers a viscosity-related torque onto the inner cylinder, which would actuate rotation. The torque is then found by determining what theoretical counterbalancing torque is necessary to hold the inner cylinder in place. For identical Newtonian liquids, the CS- and CR-rheometers with Searle and Couette systems will produce equivalent viscosity curves [21].

A coaxial cylinder viscometer, as described in U.S. Pat. No. 5,905,196 (Parshall), induces the shear of sample fluid between two concentric cylinders resulting in a laminar flow condition, and the sample viscosity is determined based on the torque exerted on the inner cylinder due to the viscous forces it endures [23]. These rheometers are suitable for a broad range of shear rates, temperatures and viscosities [21]. Most commercially-available coaxial cylinder viscometers require sample volumes of 5 to 50 mL [21].

Cone/plate rheometers allow for rapid viscosity measurements by subjecting the liquid sample to uniform shear rates [24]. Cone/plate viscometers are usually preferred over coaxial cylinder viscometers when cleaning the sample at the end of the test is an issue, as cleaning coaxial cylinder viscometers is much more time-consuming [24]. Furthermore, cone/plate rheometers generally require smaller sample volumes than coaxial cylinder viscometers [21]. Parallel plate viscometers generally require a larger sample volume compared to a cone/plate system [21].

2.2.2 Capillary Viscometer

There are two groups of capillary viscometers: absolute (which have a length/diameter ratio of 30/1 or higher) and relative (which have a length/diameter ratio of 1/1 to 10/1) [21]. Within these two groups, a further distinction can be made between capillary viscometers where the driving force used to impel the liquid through the capillary is either provided by a plunger or by gravity [21]. For a variable pressure capillary viscometer, which utilizes a piston to drive the sample through a capillary at a programmed flow rate, the flow resistance results in a pressure drop between two points spaced apart by length ΔL , which is measured by pressure transducers [21]. The viscosity is found by presetting and measuring either ΔP or flow rate Q and knowing a specific instrument constant related to the capillary dimension [21].

For capillary viscometers, which use gravity as the driving force, usually in the form of U-tube viscometers, the dynamic viscosity is proportional to the time taken for the liquid to flow between two specified points on the tube. Examples of capillary-tube-based viscometers are described

in U.S. Pat. No. US 9,733,174 B2 (Morhell et al.) and No. 6,898,963 B2 (Irani). Capillary viscometers, however, have issues with regards to cost (as you cannot use the same tube for all viscosities), cleaning (challenging to clean the capillary), and they cannot easily manipulate the rate of strain.

2.2.3 Falling Ball Viscometer

Finally, a falling ball viscometer, often used for transparent Newtonian fluids, operates on the principle that the time taken for a sphere of a given composition to fall through an inclined tube filled with the sample fluid is positively correlated with the fluid's viscosity. As the ball accelerates from rest at the top of the sample down to a distance L , it reaches steady state, which provides a uniform shear flow of the liquid [21]. The standard volume is approximately 40 mL [21].

2.2.4 Summary

For many applications, one of the most pressing requirements of the above viscometers is the volume of the sample fluid for running a test. Commercial viscometers often require a working volume ranging from 0.5 mL up to 500 mL, which can be an issue if the available volume of the fluid is insufficient to begin with (for example, as the viscosity of tears is tested, yet the collectable volume of the tear sample is under 10 microliters), or multiple measurements are required but too costly to perform (especially when it comes to rare fluids such as some offshore hydrocarbons, cerebrospinal fluids, protein-based therapeutics and biological fluids).

Therefore, there is an essential need to have an apparatus and a method to work with fluid samples with low volumes (on the order of microliters) while fulfilling the viscosity measurement. Moreover, it would be advantageous if the relevant measurement time, instrument cost, maintenance cost, and space required could be reduced or no calibration fluids were required during each assay [US. Pat. No. 6,681,616 B2 (Spaid *et al.*)].

2.3 Microfluidic Viscometers

To that end, a microfluidics-based viscometer has enormous potential in bridging the volumetric gap between a minute available sample and that required by a viscometer. Microfluidics is the science and technology that deal with systems of integrated microchannels [25] (constrained to

width/height scales between 100 nm – 100 μ m) [26] that transport and precisely manipulate small volumes of fluid (usually 10^{-9} – 10^{-18} L) [25]. Microfluidics was initially developed with the goal of miniaturizing bio-/chemical analyses. To date, there have been myriad applications of this technology platform in capillary electrophoresis, liquid chromatography, chemical reaction and synthesis, biochemical assays, etc. Some benefits of using microfluidics include, but may not be limited to, low reagent consumption, faster reaction times, and lower cost [27].

Biomedical diagnostics is considered a major application field of microfluidics, where small quantities of fluids and biological samples are transported through microchannels and can be treated and analyzed. Different biological samples like saliva, blood, sweat, urine and cerebral fluids can be used with microfluidic point-of-care devices [28]. A microfluidic system has a series of components that perform certain generic functions: a method of introducing samples and reagents into the chip, a method for transporting or mixing fluids, and other devices (like detectors) [29]. Two important developments in the field of microfluidics are creating prototype devices using soft lithography with PDMS and the ability to construct pneumatically-activated valves, mixers and pumps using soft lithography [29].

2.3.1 Pressure Sensing Microfluidic Viscometers

A pressure-sensing-based microfluidic viscometer measures a pressure drop over a straight microchannel with a known flow rate. The pressure can be measured over the microchannel in three different ways: (1) embed pressure sensors into the base of the microchannel [30]; (2) pressure sensors tapped to the side of the channel [31]; and (3) mounting an external pressure transducer downstream of the microchannel [32]. The most commonly investigated is the embedded pressure sensors; however, such viscometers are not disposable and require cleaning protocols [32].

2.3.2 Surface Tension Microfluidic Viscometers

Surface tension-based microfluidic viscometers depend on capillary pressure and surface wetting to pull liquids through a microchannel [32]. The advancing interface is tracked over time, allowing measurement of the viscosity and shear rate [32]. For Newtonian fluids, the viscosity is obtained using the Hagen-Poiseuille equation:

$$\mu = \frac{d^2}{S} \frac{\Delta P}{v(t)L(t)}$$

where d is the channel depth, $v(t)$ is the velocity of the sample front, $L(t)$ is the instantaneous length of the sample inside the capillary, S is a geometry-specific constant, and ΔP is the capillary pressure.

2.3.3 Summary

The current state of microfluidic viscometers presented in literature has one or more issues with them, which the microfluidic viscometer in this thesis will try to address. Existing microfluidic viscometers either do not measure shear-rate-dependent viscosity [33], or they require relatively large sample volumes (over 11 microliters), utilize PDMS (soft porous material causing channel deformation and absorbing sample materials); or they have only been tested using Newtonian fluids.

2.4 Research Objective

The objective of this thesis is to design a microfluidic viscometer to measure tear film viscosity (or suitable tear film alternatives). The context of the research is to enable the investigation into whether tear film viscosity can be a marker for dry eye disease and to enable clinicians and researchers to develop novel ocular lubricants using this device. Future developments resulting from this research may support these diagnostic comparisons between healthy and dry eye tears.

2.4.1 Research Aims

This research project aims to iteratively develop a method and apparatus capable of measuring small volumes of tear film mimics. Specifically, this involves designing a:

1. Customizable measurement platform, where the viscosity of tear mimics can be measured over a range of shear rates beyond what is capable with a commercial rheometer to what is more physiologically relevant.
2. Disposability of the microfluidic chip. Since it will be used to measure the viscosity of biofluids, it is desired that the chip be low-cost and fabricated in such a way that it can be produced in large numbers.
3. Non-deformable chip.

2.4.2 Project Objectives

This project's scope is to design a platform that measures the viscosity of fluids with a fast pressure response and can be programmed to vary the applied shear rate. The project involves achieving several objectives. First, to develop an understanding of the rheological properties of tear films using artificial tears. This involves investigating its viscosity dependence on shear rate and temperature. Furthermore, because tear films are not purely aqueous, an understanding of how to deal with them (e.g., surface coatings to reduce adsorption onto the channel wall and calculating interfacial tension contribution). Next, a proof of concept for the microfluidic viscometer must be developed. This will be done in part by comparing the viscosity of Newtonian liquids measured using the microfluidic viscometer to a commercial cone/plate rheometer and iteratively changing the design until the two agree. Finally, the system will be developed, and non-Newtonian fluids in the form of artificial tears will be used to validate. A graphical overview is presented in Fig. 1.

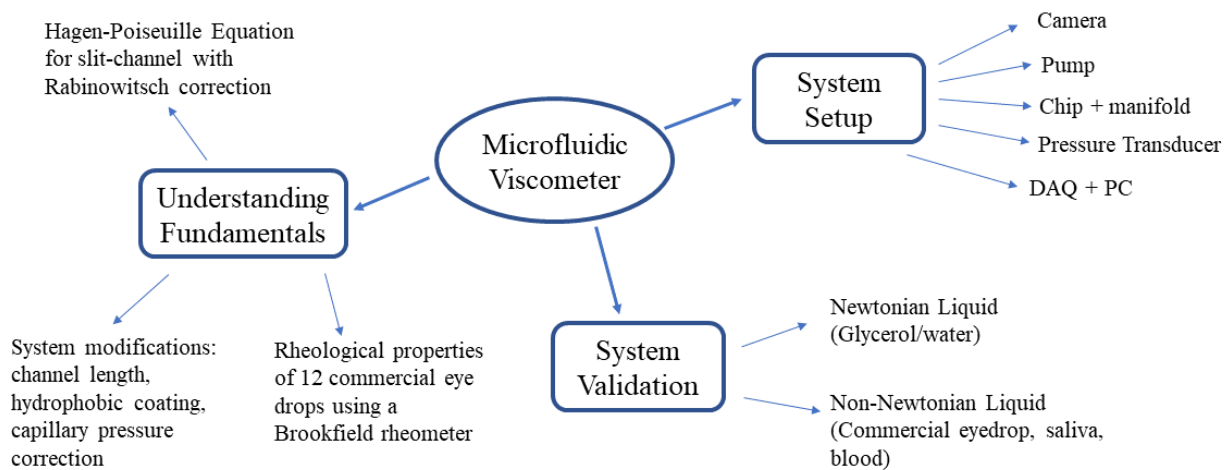


Figure 1. Microfluidic viscometer overview

Chapter 3

Methodology

3.1 Rheology Measurement Method

The experimental method is to measure the change in pressure across the sample, volumetric flow rate, sample length, and receding dynamic contact angle as the sample moves through the microchannel of an optically clear microfluidic chip in order to estimate the sample viscosity over a range of shear rates. The sample is driven, via compressed air, through the microchannel, which is fabricated in an acrylic chip. The acrylic chip allows optical access to record and observe the sample flow properties.

3.1.1 Design Principle

The design of the viscosity measurement platform began with fabricating a microfluidic chip with a loading channel, two pressure ports placed approximately 100 mm apart along the microchannel and an outlet port. This chip is housed in a 3D printed manifold that acts as the interface between the pressure ports on the chip a differential pressure transducer. The manifold also connects the microfluid chip to the syringe pump, allowing control over the shear rates. Additional supporting devices are used to capture and later analyze the flow of the sample through the optically clear microchannel. These include a DC power supply, which supplies power to the pressure transducer; a video camera, which captures the sample moving through the channel, allowing the calculation of volumetric flow rate, shear rate and capillary pressure; and finally, a computer equipped with a DAQ card. A schematic of the proposed microfluidic viscometer is given in Fig. 2.

The viscosity of the liquid sample is found using a modified version of the Hagen-Poiseuille equation for slit flow. For Newtonian liquids (where viscosity is independent of shear rate), the true shear stress and shear rate of the sample at the wall is:

$$\text{Shear Stress: } \tau_w = \frac{H(P_{\text{measured}} - P_{\text{capillary}})}{2\left(1 + \frac{H}{W}\right)L_{\text{sample}}}$$

$$\text{Shear Rate: } \dot{\gamma}_w = \frac{6Q}{\left(1 + \frac{H}{W}\right)WH^2}$$

This means that the viscosity of Newtonian liquid samples in the proposed microfluidic viscometer is:

$$\mu \text{ (Pa s)} = \frac{\tau_w}{\dot{\gamma}_w} = \frac{WH^3}{12 L_{sample}} \frac{1}{Q} (P_{measured} - P_{capillary}), \quad \text{when } \frac{H}{W} \ll 1$$

Where W is the main microchannel width, H is the main microchannel height, L_{sample} is the sample plug length, $P_{measured}$ is the measured change in pressure across the sample using a pressure transducer, $P_{capillary}$ is the calculated capillary pressure, and Q is the calculated volumetric flow rate of the sample.

When the sample is a non-Newtonian liquid, a further correction must be made to the shear rate term, known as the Weissenberg-Rabinowitsch-Mooney equation:

$$\dot{\gamma}_w = \frac{\dot{\gamma}_a}{3} \left[2 + \frac{d(\ln \dot{\gamma}_a)}{d(\ln \tau_w)} \right]$$

Where the apparent shear rate ($\dot{\gamma}_a$) is as before: $\dot{\gamma}_a = \frac{6Q}{WH^2}$.

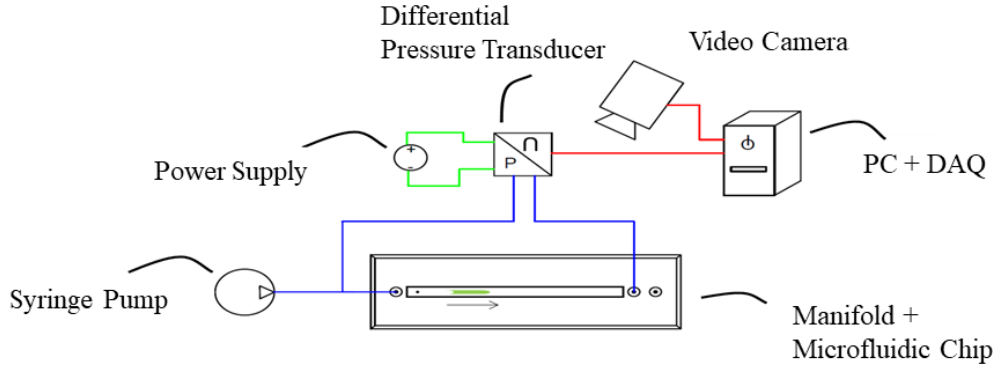


Figure 2. Schematic of the proposed microfluidic viscometer.

3.2 Materials and Fabrication

3.2.1 Microfluidic Chip

The microfluidic chip (Fig. 3a) is made up of four laser-cut layers (Fig. 3b) that are manually assembled. Each layer was designed in AutoCAD, converted into .dxf file format, and then cut through each layer with a CO₂ laser cutter (Model: VLS2.30DT, Universal Laser Systems, Scottsdale,

AZ, USA) using the relevant speed outlined in Appendix A. Layer one of the microfluidic chip is a 1.6 mm thick cast acrylic sheet (McMaster-Carr, Elhurst, IL, USA). Layer two, which is the main channel layer, is an ~134-micron thick double-sided acrylic adhesive (ARcare 90106NB, Adhesives Research Inc., Glen Rock, PA, USA). Layer three, which contains the sample loading channel, is made up of a 1.6 mm thick cast acrylic sheet (McMaster-Carr, Elhurst, IL, USA) and a 100-micron thick double-sided acrylic adhesive (McMaster-Carr, Elhurst, IL, USA). Finally, the cover film is a ~100-micron thick polyester layer (8187K12, McMaster-Carr, Elhurst, IL, USA). The microfluidic chip is held together using alternating layers of double-sided adhesive. Appendix A outlines the complete fabrication recipe for the microfluidic chip.

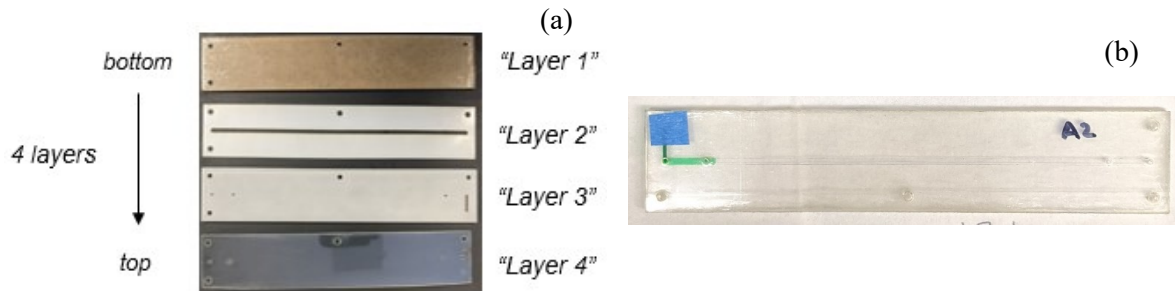


Figure 3. Microfluidic chip: (a) four laser cut layers of the microfluidic chip; (b) assembled microfluidic chip

Guide holes were manufactured into each layer to allow for more accurate assembly. The main channel has a length of 100 mm and a height of ~134 μm , allowing the channel to be approximated as a slit. In its current embodiment, the microfluidic chip has five ports. The first, at the top of the loading channel, is where the sample can be pipetted into the chip. Along the main channel, there are four additional ports. From left to right (Fig. 4): port 2 is connected to the syringe pump and one terminal of the differential pressure transducer via a 3-way junction; port 3 is used as a visual marker that the sample is loaded to and is sealed during operation; port 4 is connected to the second terminal of the differential pressure transducer; port 5 is open to atmosphere. The dimensions of each feature are given in Table 2.

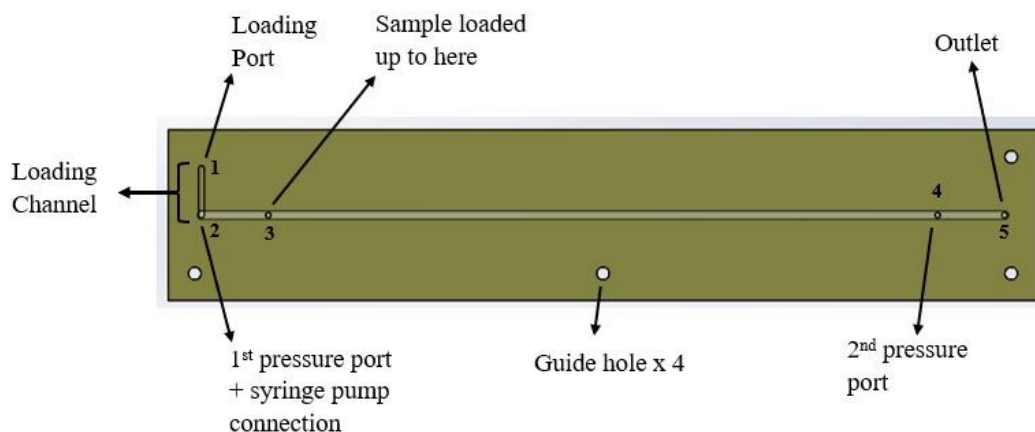


Figure 4. Main components of the microfluidic chip

Table 2. Dimensions of the Main Features of the Microfluidic Chip

Feature	Dimension [mm]
Loading Channel	7.0 x 0.8 x 1.7
Main Channel	120 x 1.26 x 0.134
Ports 1-5 (cover layer)	Diameter: 0.8 Depth: 0.1
Guide Holes	Diameter: 1.9 Depth: 3.534
Chip (outer dimensions)	130 x 25.4 x 3.534

Acrylic was chosen as the primary material for the microfluidic chip because it satisfies key criteria for measuring viscosity within the proposed system. Firstly, the acrylic sheets used are optically clear, allowing filming of the sample plug as it moves through the microchannel, which is necessary to obtain information about the sample length, sample velocity (which is correlated to volumetric flow rate), and receding dynamic contact angle. Secondly, acrylic is compatible with laser cutting. This method of fabrication was chosen over other common microfluidic chip fabrication methods (like soft lithography or 3D printing) because it allows for batch fabrication, as several chip layers can be laser cut out of one sheet of material at a time. The drawbacks of using 3D printing to

fabricate these chips are the extensive post-processing steps (eg. dissolving supports and curing), and the need to treat the chip with an automotive clear coat to render the chip optically clear enough to visualize the sample plug. Furthermore, the microfluidic chip is intended to be a consumable product, so avoiding soft lithography and its associated high equipment cost will reduce the overall cost of the chip. In addition, as will be discussed in Chapter 5, the viscosity is proportional to the cube of the channel height, which means a rigid chip with low compliance is necessary. PDMS is therefore not an ideal material within this setup.

The length of the microchannel is an important consideration insofar that it allows the sample to approach a quasi-equilibrium state, indicated by constant sample velocity. Initially, a set of chips with microchannel lengths of 61.5 mm was created and tested with the system. The total required sample volume for these chips was $\sim 23 \mu\text{L}$. These chips did not allow the sample to approach equilibrium, as the sample velocity continued to increase over the length of the microchannel. A new set of chips was fabricated with the maximum allowable microchannel length of ~ 120 mm. The length of this second set of chips was limited by the maximum allowable length of the 3D printed manifold (to be discussed below), which in turn was constrained by the 3D printer stage. Nonetheless, it was found that these chips were sufficiently long to allow the sample to approach constant velocity over the last few seconds of the test.

Once the microfluidic chips were created, they were visualized under an optical microscope at 4X magnification, and it was observed that there was distinct channel roughness caused by laser cutting. This can potentially increase sample drag, leading to an overestimation of the shear stress and, ultimately, viscosity. Because of this, a hydrophobic Aquapel Glass Treatment coating was used to smooth out the channel walls. A modified protocol based on the one outlined in “Drop-Seq Laboratory Protocol, Steve McCarroll’s Lab, Harvard Medical School” [34].

1. Using a syringe, inject Aquapel into the channel through port 1 while keeping ports 2 – 4 sealed. Let sit for 60 seconds.
2. Flush out the channel with air
3. Repeat steps 1 and 2
4. Bake chip at 65°C for 20 minutes

After channel modification, the chip was again visualized under a microscope, and it was found that the channel was rendered smooth. In addition, images of the channel were taken at three

different sections of the chip, and ImageJ was used to determine the average channel width and standard deviation. The microscope was calibrated to 1.773 $\mu\text{m}/\text{pixel}$. For the chip used in the analysis in Chapter 5, it was found that the microchannel had an average width of 1.46 ± 0.02 mm.

3.2.2 Manifold

The microfluidic chip is secured within a 3D-printed manifold (Fig. 5), which serves as a platform to connect the microfluidic chip to the syringe pump and the differential pressure transducer. The manifold was designed in SolidWorks, printed using an SLA 3D printer (Model: Form 3+, Formlabs, Somerville, MA, USA) with white resin, and cured for 30 mins at 60°C. The bottom piece of the manifold was designed with a groove that allows the microfluidic chip to sit securely in place. It also features an elevated rim so that the through-holes in the manifold cover are lined up with the ports on the microfluidic chip when the chip is loaded. The manifold cover contains 1/8" nominal ID O-rings around each through-hole so that when the manifold is closed, an air-tight seal around the microfluidic ports is formed. The outer side of the manifold cover (not pictured) was tapped using a #3 drill to produce 1/4-28 threads. This was needed to screw in the three flangeless peek fittings (Model: XP-283, IDEX Health & Science, Oak Harbor, WA, USA), which hold in place 1/16" OD stainless steel tubing (Model: SS-T1-S-020-20, Swagelok, Cleveland, OH, USA). Thus, the ports on the top of the manifold were designed so that their depths were roughly equal to the depth of the thread of the fitting, and their radii were proper to allow tapping to produce the threads matching that of the chosen fitting. Below these large ports, smaller pinholes were designed with a depth of approximately 5 mm to provide stability to the manifold when the fittings were being screwed in and with radii comparable to that of the ports on the microfluidic chip.

The design specifications for the manifold are that it can hold the microfluidic chip securely and form air-tight seals with ports 2, 4, and 5. Furthermore, since it was found that the flow rate programmed into the syringe pump was not the on-chip volumetric flow rate of the sample, a method to calculate this via post-processing was established. For that reason, the manifold was designed with a viewing window in the cover for flow rate and capillary pressure determination.

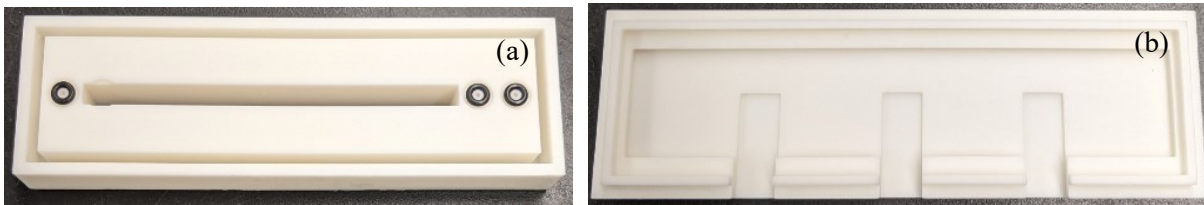


Figure 5. 3D printed manifold: (a) cover; and (b) base

3.3 Characterization

3.3.1 Pump

The selected pump used within this microfluidic viscometer setup was chosen to give precise control over the volumetric flow rate, and be capable of being integrated with LabVIEW 2020. The chosen pump was Harvard Apparatus Pump 11 Elite (Model: PROG DUAL, Harvard Apparatus Canada, St. Laurent, QC). It is compatible with a Hamilton 1000 Series Gastight Syringe: Luer Lock (Model: 1001, Thermo Fisher Scientific, Mississauga, ON). The pump was connected to the PC via USB connection, and a LabVIEW VI was created to start its fusion subroutine along with the pressure data acquisition. The pump offers high accuracy, up to 1.28 pL/min, which is substantially lower than what was required to overcome the static frictional forces of the sample to produce movement. Furthermore, the minimum pusher travel rate for this pump was 0.18 $\mu\text{L}/\text{min}$. For the tests conducted with Newtonian and non-Newtonian liquids, the flow rate programmed into the pump was on the order of 10^1 to 10^2 $\mu\text{L}/\text{min}$. Therefore, the error contribution from the pump with regards to the volumetric flow rate of the sample within the microchannel is negligible.

3.3.2 Differential Pressure Transducer

The chosen differential pressure transducer is tied to the exact specifications of the data acquisition (DAQ) device used in the PC to collect voltage signal from the pressure transducer and converts it to a digital one. The DAQ used was a PCI-6221 Multifunction I/O Board (National Instruments, Austin, TX). The LabVIEW VI used for collecting pressure data was set to a sampling frequency of 1 kHz. Ideally, the DAQ should have a sampling rate of 10 times this value. The PCI-6221 has a maximum sampling rate of 250 kS/s, which is adequate. Furthermore, the DAQ should have an analog input resolution less than the pressure transducer's output resolution to capture all of

the pressure fluctuations. The DAQ supports an analog input range of ± 5 V with 16-bit analog input resolution. This means that the minimum voltage change that the DAQ can detect is $\frac{5V - (-5V)}{2^{16}} = 152 \mu V$.

The differential pressure transducer chosen was a ± 10 in H_2O analog board mount differential pressure transducer (Model: HSCDRR010NDAA3, Honeywell Sensing and Productivity Solutions, Charlotte, NC). It has an output resolution of 0.03% FS (full scale). Therefore, the minimum pressure change it can register is $20 \text{ in } H_2O * 0.03\% = 0.006 \text{ in } H_2O$. Using the transfer function in the datasheet, $V_{out}(0 \text{ in } H_2O) - V_{out}(0.006 \text{ in } H_2O) = 1.650729 \text{ V} - 1.65 \text{ V} = 792 \mu V$. Therefore, the analog output resolution of the differential pressure transducer used is greater than the DAQ's analog input resolution, meaning this transducer is suitable for use in this setup.

Before using the differential pressure transducer in the setup, its input pressure to output voltage scaling parameters must be identified for use in the LabVIEW VI to obtain meaningful pressure readings. To do this, the two radial barbed ports of the transducer were connected to an MFCS-EZ Microfluidic Flow Control System (Fluigent, Le Kremlin-Bicêtre, France). The pressure controller supplies a known setpoint pressure across the two terminals of the transducer, and the subsequent voltage output was recorded (Fig. 7). The equation relating the input differential pressure to the voltage output of the pressure transducer was then: $\Delta P[\text{in } H_2O] = 7.2304 \text{ V} - 12.101$. These scaling parameters were then plugged into the LabVIEW.

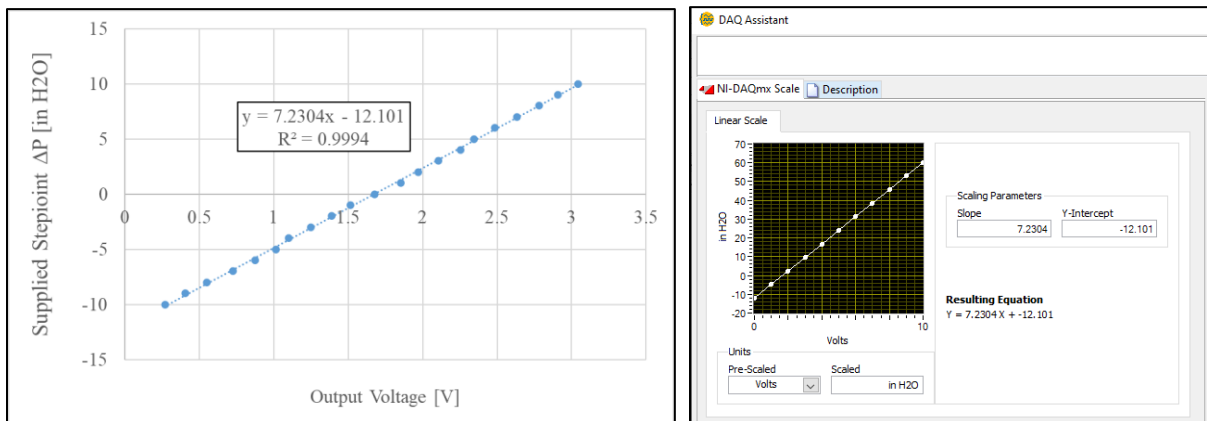


Figure 6. Pressure-Voltage Scaling Parameters: (a) Relationship found using flow controller; and (b) NI-DAQmx inputs

The pinouts for the differential pressure transducer are given in Fig. 5. Pin 2 is V_{supply} and is connected to a DC power supply, supplying a voltage of 3.3 V. Pin 3 is V_{out} and is connected to port 1 of the I/O Terminal Block (Model: CB-37F-LP, National Instruments, Austin, TX), which connects to the DAQ via a 37 pin D-SUB connector. Pin 4 is the ground.

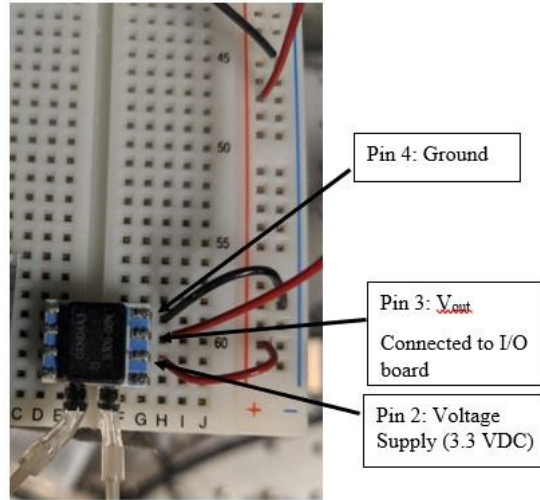


Figure 7. Differential pressure transducer pinout

3.3.3 Video Camera

The video camera in this microfluidic viscometer serves dual purposes. First, it allows filming of the sample plug moving through the microchannel, which provides information about its velocity and, ultimately, the true volumetric flow rate and shear rate experienced by the sample. Secondly, as will be discussed in Chapter 5, the capillary pressure contribution must be accounted for. Therefore, the receding dynamic contact angle is necessary and can only be found via filming. The camera and lens combination, therefore, must have sufficient resolution to capture these details, must have a reasonable focal length so that it does not have to be placed too far away from the manifold/chip, and must be able to capture video with high enough frame rate so an accurate velocity profile can be obtained.

A camera survey was conducted, and it was found that a 5 MP SONY IMX264 Enclosed Color USB3 CMOS Camera (Model: PL-D795CU, Navitar Inc., Rochester, NY) was suitable. A balance was reached between an appropriate resolution (5 MP), the largest pixel size or photosite area available ($3.45 \mu\text{m} \times 3.45 \mu\text{m}$), the camera's overall size and weight, and its cost. Ideally, for a given

resolution, a larger pixel size is desired as this results in a better digital signal and a larger dynamic range and tonal clarity. This equates to less noise. Progressive CMOS or CCD cameras were both available, but CMOS was preferred as the readout is considerably faster. Finally, when choosing a lens, the size of the lens must be greater than or equal to the size of the camera sensor or else the whole image will not be captured. Therefore, a 5 mm F/2.8 2/3" Megapixel C-Mount lens (Model: NMV-5M23, Navitar Inc., Rochester, NY) was chosen.

Prior to filming the sample, the perspective shift of the camera must be determined and quantified. For this, lines of known length are drawn on the top side of the microfluidic chip, and a picture is taken of it using the camera. The correction coefficient is calculated by:

$$C = \frac{L_{known}}{L_{captured}}$$

where L_{known} is the known length of the line drawn on the microfluidic chip and $L_{captured}$ is the length of the line in the captured image. When the fluid sample length is to be calculated, the measured length from the image must be multiplied by this correction factor to account for the visual bias of the camera. If the camera is ever shifted away relative to the manifold, it changes the visual bias correction coefficient, which must then be re-evaluated.

Chapter 4

Shear-Thinning and Temperature-Dependent Viscosity Relationships of Commercially Available Eye Drops [4]

Due to a lack of ability to source human tears from patients with healthy eyes and sufferers of dry eye disease, the rheological properties of a suitable alternative in the form of artificial tears (or eye drops) were investigated. The objectives of this study were to understand how to deal with the eye drops in this system eventually, to understand their viscosity profiles, and to determine certain key factors that influence their viscosity profiles, namely the dependence on the shear rate and temperature of the artificial tears. Furthermore, the viscosity information for common, contemporary over-the-counter eye drops is not readily available and is often not provided by the manufacturer.

4.1 Ocular Lubricants

Dry eye disease causes a disruption in the tear film leading to damage to the epithelial cells, which can cause further irritation [1]. In addition, during the natural process of cell repair and replacement, the ocular surface is susceptible to further damage [1]. One of the first-line treatments for DED is the use of ocular lubricants (also commonly referred to as artificial tears or eye drops) [9], [35]. This is because they are noninvasive and result in minimal adverse side effects [13].

Artificial tears are complex polymer solutions composed of electrolytes, surfactants, lubricants and preservatives that, on application, spread evenly over the ocular surface to provide the wearer relief from inflammation and reduce friction between the eyelid and the cornea during blinking [1], [36]. They serve a multitude of purposes from lubrication, removing debris, supplementing tear film components and reducing pro-inflammatory mediators [13]. Artificial tears generally contain a water-soluble polymer that serves the function of increasing residence time, improving hydration, and attachment to the inner mucous layer, which can promote corneal healing [37]. In addition, using artificial tears has demonstrated the ability to alleviate the subjective and objective signs of DED [1], [13].

Manufacturers typically vary the physical properties of artificial tear formulations by using different lubricants, thereby changing their mechanism of action [1]. Along with formulation differences, the wide variety of commercially available eye drops, as reported by Miler *et. al.*, are

distinguished by their “viscosity, type of electrolytes used, pH, osmolarity and presence or lack of a preservative” [13]. The complex interaction between the lipid components of the tear film and the ingredients in artificial tears likely influence overall tear stability [16]. Users generally tend to choose an artificial tear formulation based on a qualitative assessment of its comfort, blur potential once instilled onto the eye, and reduction of dry eye symptoms [38]–[44].

Artificial tears only provide short-term relief upon administration because they are rapidly removed from the ocular surface through tear drainage, non-productive absorption, and blinking [44]–[49]. Furthermore, there is a physical limit to the volume of tears that the cul-de-sac can hold, which is typically $30\mu\text{L}$, and any overflow amount is drained away [50]. To increase the residence time and bioavailability of artificial tears, one strategy is to increase the viscosity of the formulations using high molecular weight polymers [50].

Much like the shear-thinning nature of the tear film, artificial tears are designed to have increased viscosity at lower shear rates (like in between blinks when the eyelid is relatively stationary), which is intended to enhance its retention and optimize its hydrating and protection capabilities [13], [37]. An artificial tear with increased viscosity can also help patients suffering with goblet cell loss [13]. Conversely, at high shear rates, in order to improve comfort and reduce stickiness and blur, the artificial tears should have a lower viscosity [37]. While increasing viscosity improves residence time, it also can create several problems such as discomfort and blurring. In theory, the ideal formulation should be viscous at low shear rates, such as when the eyes are opened, to prevent removal of the lubricants from the ocular surface [51]. Users who suffer from incomplete blinking or an irregular positioning of the eyelids may have an extended interblink interval, which can cause instability of the tear film and exacerbate the symptoms of DED. Artificial tears, in this case, can be used to counteract this phenomenon by providing hydration and reducing the presence of proinflammatory mediators [13].

Finally, temperature has a significant effect on the viscosity of artificial tears [7]. In general, as the temperature of a non-Newtonian fluid is increased, its viscosity decreases [52]. For instance, the viscosity of an eye drop will be lower at ocular surface temperature than if it was stored in a room-temperature bottle [53]. Additionally, some clinicians advise patients to store their eye drops in the fridge (at approximately 4°C) for more pronounced relief of dry eye symptoms upon insertion, due to its cool sensation.

4.2 Materials and Methods

A total of 12 commercially available eye drops (Table 1) were evaluated in this study. The selection of these eye drops was made in such a way as to provide a wide range of viscosities from around 1 to above 100 mPa·s. This wide range of viscosities available in commercial eye drops affords users a range of choices depending on their individual severity of DED. Shear viscosity was measured by using a cone/plate rheometer (Model: LVDV-III+, Brookfield Engineering Laboratories Inc, MA, USA) equipped with a standard cup and an RTD temperature probe (Model: SC4-61Y) (Fig 1). The two customizable components of the rheometer are the cup (Model: CPA-44YZ) and the spindle (CPA-40Z). The reported range of this spindle is 0.15 – 3,065 mPa·s. The spindle made a cone angle of 0.8° with the bottom plate and had a cone radius of 2.4 cm. The rheometer's built-in electronic gap setting feature was used to establish a 0.0005-inch spacing between the cup and the spindle every time the spindle was attached.

Using a micropipette, 0.5 mL of the sample was collected and deposited into the cup. The temperature displayed on the rheometer was recorded. For each shear viscosity measurement, the spindle rotation speed (revolutions per minute, RPM) was manually inputted and the resulting torque (%), viscosity (mPa·s), shear stress (N/m²) and shear rate (s⁻¹) were calculated and displayed by the rheometer and then recorded. To ensure a valid measurement, the torque reading needed to be between 10% and 100%, as per the instructions from the rheometer manufacturer. Therefore, every time a new type of eye drop was tested at a given temperature, the upper and lower RPM bounds needed to be established by trial-and-error to ensure that the resulting torques met the above criterion. Eight more RPM values were chosen at roughly equal increments between the two bounds, so that a total of 10 measurements at various shear rates for each sample per test are projected. Three tests were conducted for every eye drop sample at each of the three temperatures. The average value of the measured viscosities at each shear rate under a specific temperature was employed for analysis. Before a new eye drop sample was measured, the cup and spindle were both rinsed with distilled water and isopropyl alcohol and then air blow-dried.

The cone/plate rheometer induces a rheologically-controlled flow within the sample, and measures its mechanical response to the shear deformation imposed by the rotating cone [54]. More specifically, the cone is attached to a calibrated spring, which deflects as a result of the viscous drag of the eye drop solutions [55]. As the cone spins with a given angular velocity, the velocity field

within the sample approaches steady-state [54], and the angular velocity is converted to the desired rheological parameters. The angular speed of the rheometer is linearly correlated to the shear rate as shown below, $RPM = \frac{\dot{\gamma}}{7.5}$. Five full rotations of the spindle were allowed before recording a measurement.

Shear viscosities were obtained at three clinically relevant temperatures at which users may experience exposure to the drops. Most eye drops are stored and applied at room temperature ($\sim 24.6^\circ\text{C}$); however, some eye care practitioners advise their patients to refrigerate their eye drops before application, resulting in eye drops that have temperatures close to 4.3°C . Finally, on application, eye drops will heat up to the ocular surface temperature ($\sim 34.5^\circ\text{C}$). In order to regulate the temperature of the measured eye drop, two different bath circulators were connected to the rheometer cup. The hot water bath (Model: SC150-S45, Thermo Fisher Scientific) was filled with DI water and the refrigerated bath circulator (Model: mx 71 r-20, VWR International) was filled with glycerol solution. The large thermal mass of the liquids in the circulator tanks were used to passively maintain the sample temperature. Understanding the shear viscosity information at these three temperatures is therefore important when prescribing eye drops for treating dry eye disease or for developing new formulations. For measuring the eye drops at ocular temperatures and 4.3°C , bath circulators were connected to and utilized with the rheometer (Fig. 8) to control the temperature of eye-drop samples.

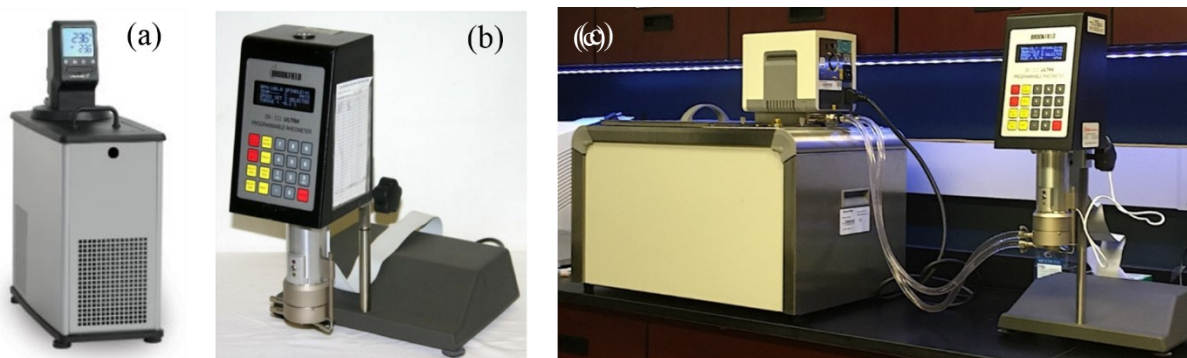


Figure 8. The shear viscosity measurement setup: (a) the rheometer; (b) a refrigerated bath circulator (model: mx 71 r-20, VWR International); and (c) a warming bath circulator (left; model: SC150-S45, Thermo Fisher Scientific) connected to the rheometer.

4.3 Results

The shear viscosities of 12 commercially available eye drops were measured at three different temperatures at the minimum and maximum shear rates allowed by the rheometer, with $n = 3$ trials conducted at each temperature. Based on rheological analysis (Fig. 9), the shear-thinning behavior for all eye drops tested at each of the three temperatures was identified. In general, for the same sample at approximately the same shear rates, the measured shear viscosity increased with decreasing temperatures. At room temperature, Refresh Optive Gel Drops (Allergan Inc.) had the highest viscosity (106.23 mPa·s) at the lowest measurable shear rate (2.25 s⁻¹), and Systane Balance Lipid Layer Formula (Alcon Laboratories Inc.) had the lowest viscosity (2.25 mPa·s) over the lowest measurable shear rate (120 s⁻¹).

There was a distinct temperature response in the measured shear viscosity and shear rates. In all samples, as the temperature decreased, the viscosity curve shifted upwards, and the flow consistency index K (that is, the effective viscosity at 1 s⁻¹) increased. Furthermore, as the temperature decreased, the range of shear rates that the rheometer was able to render became narrow due to an increased torque for a given shear rate. It should be noted that the relative percentage change of the flow consistency index K of each eye drop differed with changing temperature. To calculate this, first, the mean overlapping shear rate for a given eye drop sample at the three measured temperatures was determined. Then, the effective viscosity of each eye drop sample at the three temperatures at this shear rate was calculated using the Ostwald-de Waele fitted coefficients, so that a relative percent change could be determined. For example, when the temperature of Refresh Optive Gel Drops (Allergan Inc.) was increased from 4.3°C to 24.6°C, a 63% decrease in viscosity was observed at a shear rate of 5.63 s⁻¹.

However, in the case of Systane Ultra Hydration (Alcon Laboratories Inc.) undergoing the same temperature change, a 49% decrease in viscosity was observed at a shear rate of 21.38 s⁻¹. Similarly, when the temperature was increased from 24.6°C to 34.5°C, the viscosities of Refresh Optive Gel Drops and Systane Ultra Hydration decreased by 30% and 23%, respectively. In general, these differences can be attributed to the type and concentration of the constitutive macromolecules and the salinity of each eye drop formulation.

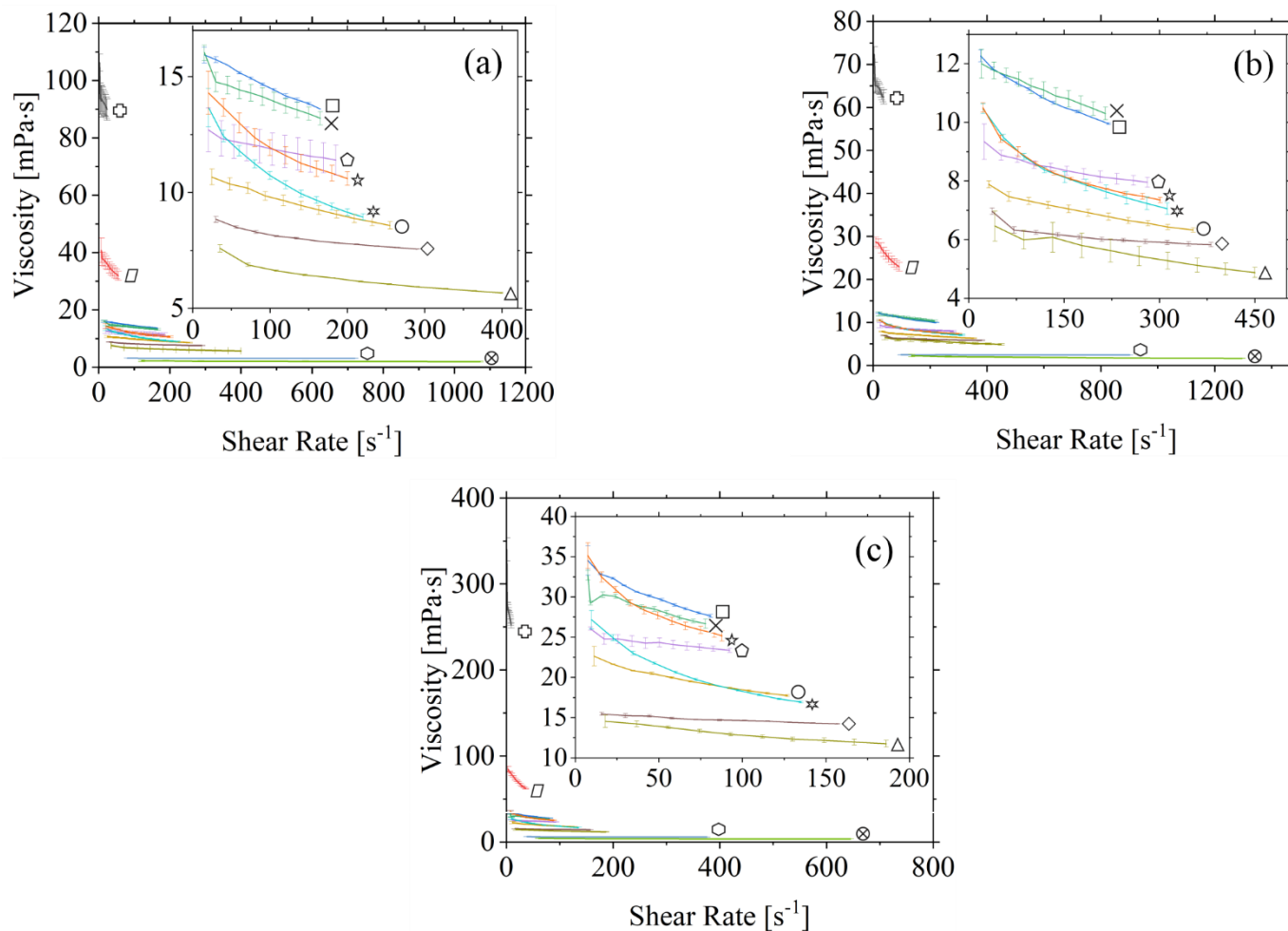


Figure 9. Shear viscosities of 12 different commercial eye drops at (a) $24.6 \pm 1.2^\circ\text{C}$, (b) $34.5 \pm 0.1^\circ\text{C}$, and (c) $4.3 \pm 0.3^\circ\text{C}$. Refresh Optive Gel Drops (*heavy cross*), Systane Ultra Hydration (*rhombus*), Refresh Optive Fusion (*square*), Blink Moisturizing Lubricant Eye drops (*X*), Bio True (*pentagon*), Long Lasting Relief (*circle*), Hylo Comod (*starburst*), Refresh Optive Advanced (*diamond*), Systane Complete (*triangle*), Systane Ultra High Performance (*star*), Thealoz Duo (*hexagon*), Systane Balance Lipid Layer Formula (*circled X*)

4.3.1 Ostwald de Wale relationship: Mathematical model

To quantify the shear-thinning behavior of the eye drops, the viscosity data can be modeled using the Ostwald-de Waele equation, which is derived from Newton's Law of Viscosity and has been generally used to describe the behavior of typical non-Newtonian fluids

$$\mu_{eff} = K(T)\dot{\gamma}^{n-1}$$

where K (equal to the viscosity at 1 s^{-1}) is the flow consistency index (Pa s^n) and is a function of temperature; and n is the dimensionless flow behavior index (the fluid is a pseudoplastic when $n < 1$) [56].

To determine the coefficients (i.e. K and n) of the Ostwald-de Waele equation, a power-law formula was used to best-fit the viscosity data of every sample (Fig. 10). Based on the viscosity data for Systane Ultra Hydration (Alcon Laboratories Inc.), the flow consistency index K was found to be $49.64 \text{ mPa}\cdot\text{s}^{0.893}$ and the flow behavior index n was 0.893, indicating that this eye drop is a shear-thinning fluid. Similarly, all 12 eye drops at each of the three studied temperatures were analyzed, and the two corresponding characteristic indices have been obtained. Table 3 lists the coefficients for each of the 12 samples at each of the three temperatures.

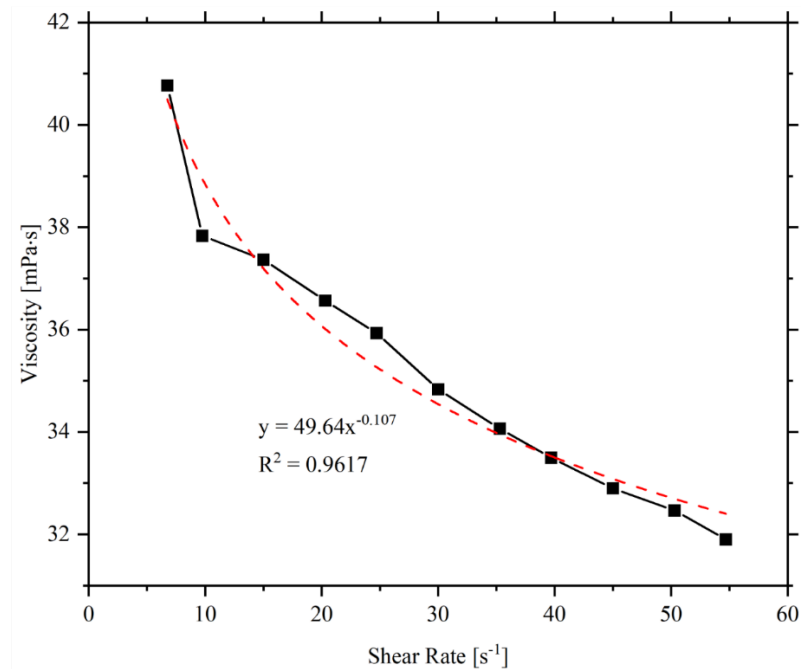


Figure 10. The power-law fitting (dashed line) of the sheasar viscosity data of Systane Ultra Hydration (solid line) at room temperature, where K and n are $49.64 \text{ mPa}\cdot\text{s}^{0.893}$ and 0.893, respectively.

It is noted that the coefficients of the Ostwald-de Waele relation are explicitly relevant across the range of shear rates under which the measurements were conducted. Therefore, care must be taken when attempting to extrapolate the viscosity values at more physiologically relevant shear rates.

Other widely used mathematical models (like the cross and sisko models) [57] could have been used to fit the viscosity evolution against shear rates, but these models require an infinite shear viscosity (η_{∞}), which can only be found via plotting the data in a logarithmic manner (ie. by a log-log plot) and locating the second Newtonian plateau [58]. However, due to limitations in the range of shear rates rendered by the rheometer, this value was unable to be obtained. Thus, a power-law model was chosen and used to fit all the data. The R^2 value, which is a quantitative correlation coefficient between the model and the measured data, indicates that the power-law model has accurately described the relation of the shear viscosity and the shear rate. Formulating a mathematical model will allow for the validation of eye drops using the microfluidic viscometer, as the expected viscosity can be calculated based on the observed shear rate of the sample in the microchannel.

Table 3. Ostwald-de Waele coefficients for 12 commercial eye drops

	4.3°C			24.6°C			34.5°C		
Eye drops	K(T)	n	R ²	K(T)	n	R ²	K(T)	n	R ²
Refresh Optive Fusion	42.22 ± 2.29	0.906 ± 0.012	0.95	19.77 ± 0.57	0.926 ± 0.001	0.90	16.09 ± 0.40	0.915 ± 0.004	0.95
Long Lasting Relief	30.37 ± 1.82	0.898 ± 0.012	0.98	15.71 ± 0.70	0.903 ± 0.005	0.93	10.99 ± 0.28	0.911 ± 0.002	0.96
Refresh Optive Advanced	17.70 ± 0.51	0.964 ± 0.005	0.93	11.47 ± 0.33	0.931 ± 0.005	0.99	8.58 ± 0.18	0.932 ± 0.002	0.93
Systane Complete	21.64 ± 0.99	0.903 ± 0.005	0.95	11.40 ± 0.42	0.885 ± 0.006	0.99	10.63 ± 1.42	0.884 ± 0.015	0.91
Bio True	28.75 ± 0.62	0.960 ± 0.001	0.99	14.73 ± 1.26	0.953 ± 0.005	0.97	11.65 ± 0.87	0.935 ± 0.010	0.98
Systane Ultra High Performance	48.95 ± 2.08	0.862 ± 0.006	0.99	23.71 ± 1.79	0.863 ± 0.010	0.98	16.35 ± 0.41	0.865 ± 0.001	0.99
Thealoz Duo	6.68 ± 0.11	0.980 ± 0.001	0.73	3.40 ± 0.11	0.988 ± 0.002	0.76	2.59 ± 0.05	0.993 ± 0.003	0.87
Hylo Comod	43.72 ± 2.55	0.812 ± 0.012	0.97	26.45 ± 1.99	0.819 ± 0.013	0.98	16.98 ± 0.24	0.849 ± 0.007	0.99
Systane Ultra Hydration	106.82 ± 3.25	0.871 ± 0.006	0.97	49.83 ± 5.80	0.892 ± 0.016	0.95	37.27 ± 1.32	0.896 ± 0.002	0.90
Systane Balance Lipid Layer Formula	5.74 ± 0.44	0.925 ± 0.010	0.99	3.04 ± 0.66	0.938 ± 0.022	0.98	5.07 ± 1.30	0.856 ± 0.039	0.98

Refresh Optive Gel Drops	290.23 ± 8.01	0.908 ± 0.007	0.74	109.99 ± 4.86	0.946 ± 0.001	0.86	74.24 ± 2.21	0.950 ± 0.003	0.77
Blink Moisturizing Lubricant Eye drops	33.79 ± 0.45	0.936 ± 0.001	0.63	19.49 ± 0.52	0.928 ± 0.001	0.97	15.54 ± 0.71	0.936 ± 0.005	0.91

4.4 Discussion

The shear viscosities of common lubricants used in eye drop formulations have been shown to vary with temperature by differing amounts [59]. For example, a study by Rahman *et. al.* showed that the decrease in the relative viscosity of 0.4% sodium hyaluronate was appreciably more than 0.5% carmellose sodium when the temperature was increased from 22°C to 35°C [59]. Higher temperatures may induce greater mobility of the constituent macromolecules, leading to a decrease in the overall viscosity of the eye drop.

This study only measured the effects of temperature, shear rate, and viscosity of 12 eye drops. Further studies may need to include a wider range of available artificial tears (with and without preservatives) and look at other physiochemical properties like osmolarity, surface tension, density and molecular weight [50]. The technical limitations of this study are that the rheometer used could not measure the viscosity of the samples within a consistent shear rate range, nor could it reach shear rates up to 28,500 s⁻¹. For this reason, caution must be taken when extrapolating the results of this study beyond the measured shear rates. Furthermore, it is important to note that the *in vivo* shear behavior of these ocular lubricants has not been investigated. A separate study related to this would be beneficial to get a more comprehensive view of their rheological behaviors at a range of physiologically relevant shear rates and temperatures.

Chapter 5

Development of the System

To derive the equation that relates the apparent fluid viscosity to the measured parameters (flow rate, differential pressure across the sample, channel dimensions and sample length), some important assumptions about the fluid flow must be made. Namely, that the flow approaches an equilibrium or quasi-equilibrium condition, laminar flow exists within the microchannel, the liquid sample is incompressible, and the tests are conducted at constant temperature. The last assumption is important because, as shown in Chapter 4, the viscosity of a liquid sample has a temperature dependence.

5.1 Idea (equation)

The Reynolds number relates a fluid's inertial force to its viscous force and can indicate if the liquid is in the laminar regime. This is given by the equation:

$$Re = \frac{\rho v L}{\mu}$$

where ρ is the density of the liquid, v is the average flow velocity, L is the characteristic length, and μ is the liquid dynamic viscosity. The average flow velocity (v) is different for each test and is ultimately controlled by the syringe pump. This value is also used to calculate the volumetric flow rate of the sample (Q). Generally, v is on the order of $10^1 \frac{mm}{s} = 10^{-2} \frac{m}{s}$. The density of eyedrops is on the order of $10^3 \frac{kg}{m^3}$. Because the channel is a rectangular slit channel, the characteristic length is on the order of the channel height, which is $10^{-4} m$. Finally, the dynamic viscosity is on the order of $10^{-3} to 10^{-2} Pa \cdot s$. Putting all this together, the maximum Reynolds number for the data collected is on the order of: $Re \sim 10^{-1} to 10^0$, which indicates that the flow in the microchannel can be approximated to be within the laminar regime.

5.1.1 Theory

In general, the dynamic viscosity of a slit-channel microfluidic viscometer is calculated based on the Hagen-Poiseuille equation for fully developed slit-flow together with the Weissenberg-Rabinowitsch-Mooney correction for non-Newtonian fluids:

$$\mu = \frac{\tau_w}{\dot{\gamma}_w} = 3 \cdot \frac{WH^3 \Delta P}{12QL} \left[2 + \frac{d(\ln \dot{\gamma}_a)}{d(\ln \tau_w)} \right]$$

Where $W, H, \Delta P, Q, L$ are the channel width, channel height, differential pressure across the sample, volumetric flow rate of the sample, and length of the sample plug respectively. Furthermore, $\dot{\gamma}_a$ is the apparent shear rate at the channel wall, given by $\dot{\gamma}_a = \frac{6Q}{WH^2}$, and τ_w is the shear stress at the channel wall, given by $\tau_w = \frac{H\Delta P_{measured}}{2\left(1+\frac{H}{W}\right)L}$.

Figure 9 is a 2D representation of a sample fluid plug traveling through the microfluidic channel. Its forward motion through the channel results from a syringe pump compressing air upstream of the sample, which acts like an air piston providing sufficiently large forward force to overcome the static frictional forces. Once the sample is in motion, it encounters resistive forces in the form of interfacial tension, viscous forces and channel adhesion. When measuring the viscosity of the sample, only the viscous forces are of concern; however, the presence of the interfacial tension and the channel adhesion result in an overestimation of the calculated shear stress and, ultimately, the viscosity. A hydrophobic coating was applied to the channel to mitigate the effects of adhesion, rendering it substantially smooth. Likewise, to account for the interfacial tension, which occurs due to the presence of the air-liquid interface, the capillary pressure was calculated using captured video of the sample moving through the channel. The capillary pressure is found by the Young-Laplace equation:

$$P_{capillary} = p_0 - p_1 = \frac{2\sigma \cos \theta}{\bar{R}}$$

where σ, θ, \bar{R} are the estimated surface tension of the sample, the retreating dynamic contact angle (as portrayed in Fig. 1), and the radius of curvature of the sample. This is given by $\bar{R} = \frac{1}{\frac{1}{H} + \frac{1}{W}}$, where H and W are the channel height and width.

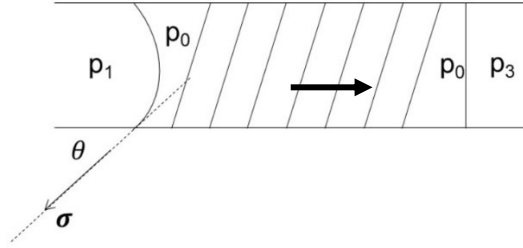


Figure 11. 2D representation of the sample plug moving through a section of the microfluidic channel

This calculated capillary pressure is subtracted from the total measured pressure ΔP to get a more representative change in pressure across the sample, and ultimately dynamic viscosity calculation. The dynamic viscosity of the fluid sample is the ratio of the shear stress and shear rate, and the true shear stress is calculated by:

$$\text{Shear Stress: } \tau_w = \frac{H(\Delta P_{\text{measured}} - P_{\text{capillary}})}{2\left(1 + \frac{H}{W}\right)L}$$

5.2 Method

At the beginning of a measurement, the sample fluid is loaded into the microfluidic chip, which is then placed in the manifold (as described previously). The syringe pump, pressure transducer data acquisition and the camera are then started simultaneously. The syringe pump has been set to a constant flow rate (between 50 to 250 microliters/min), and as the syringe plunger is pushed, the air upstream of the sample is compressed. As the air reaches a critical pressure, it forces the liquid sample to move forward through the microchannel. The flowing process of the sample is visualized, and the video is taken from above the manifold.

In theory, the propelling force for the sample, i.e., the total pressure difference created by the pump, is opposed by three forces: the viscous force (which is of interest), the drag (which is mainly caused by the channel roughness and adhesion) and the capillary force. To minimize the noising effect of the drag, a channel coating is applied to render the channel smooth and hydrophobic. Regarding the capillary force, the capillary pressure difference is calculated using the equation above and needs to be subtracted from the total pressure difference measured from the pressure transducer.

5.3 Testing Methodology

Because there is an inverse relationship between the temperature of the glycerol solutions and their viscosities, the experiments were conducted at room temperature, and the solutions were stored at room temperature. This was done to minimize temperature effects on the response variable. Furthermore, there are two broad classifications of fluids: Newtonian and non-Newtonian. Fluids in the latter group (to which tear films belong) have the property that their viscosities depend on the shear rate at which they are measured. The viscosity of Newtonian fluids, on the other hand, are not influenced by shear rate. To eliminate the effects of an additional nuisance variable (variations in the measured shear rate), glycerol solutions were chosen as test solutions. The glycerol solutions are Newtonian fluids whose viscosity depends on their weight fraction and temperature, and not on shear rate.

Their channel widths were measured using a pre-calibrated optical microscope and ImageJ at ten random points along the length of the channel. These widths were averaged to give a representative channel width for each chip. Next, four different weight percent of glycerol in water solutions were prepared (each with a different viscosity) as test solutions to see the impact of the viscosity of the test solution and the accuracy of the viscometer. The weight fractions of the glycerol solutions were chosen to span the range of viscosities one can expect with human tear films (both healthy and dry eyes). Furthermore, the interfacial tensions of the glycerol samples are needed to calculate their capillary pressure contribution. These values were taken from a study by Gladwel *et al.* [60].

5.4 Setup and Running a Test

This microfluidic viscometer (Fig. 12) is comprised of a microfluidic chip enclosed in a 3D printed manifold that serves to interface the chip with a syringe pump and differential pressure transducer, along with additional supporting devices. These include: a DC power supply, which supplies power to the pressure transducer; a video camera, which captures the sample moving through the channel, allowing the calculation of volumetric flow rate, shear rate and capillary pressure; and finally, a computer equipped with a DAQ card.

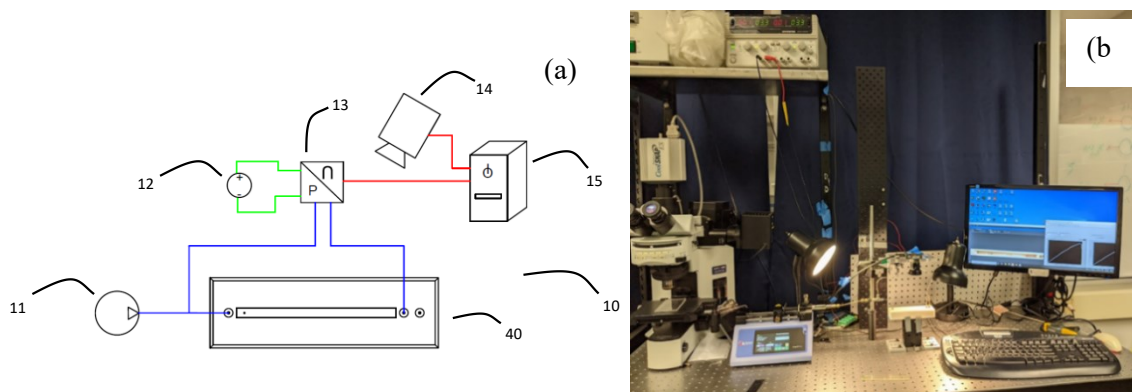


Figure 12. The microfluidic viscometer setup: (a) diagram with (11) syringe pump, (12) DC power supply, (13) differential pressure transducer, (14) video camera, (15) computer with DAQ card, (40) manifold with microfluidic chip; (b) picture.

A programmable syringe pump (Model: Pump 11 Elite, Harvard Apparatus, Holliston, MA, USA) is positioned so that an empty syringe is pneumatically connected to the first port on the main channel of the microfluidic chip contained within the manifold and one terminal of a 10-in. H₂O differential pressure transducer (Model: HSCDRRN010NDAA3, Honeywell Sensing and Productivity Solutions, Charlotte, NC, USA) via rigid PEEK and stainless steel tubing. This is achieved using a 1/16" 3-way union tee fitting (Model: SS-100-3, Swagelok, Solon, OH, USA). A 5MP CMOS camera (Model: PL-D795CU, Navitar, Rochester, NY, USA) equipped with a 2/3" MP lens (Model: NMV-5M23, Navitar, Rochester, NY, USA) is positioned directly above the manifold and the chip to take a video of the sample as it moves through the microchannel. Prior to the measurement, the perspective shift of the camera must be determined and quantified (as outlined in Chapter 3).

At the beginning of a measurement, the sample fluid is loaded into the microfluidic chip, which is then placed in the manifold (as described previously). The syringe pump is set to a constant flow rate (on the order of 10^1 to 10^2 $\mu\text{L}/\text{min}$). The syringe pump, pressure transducer data acquisition and the camera are then started simultaneously. As the syringe plunger is pushed, the air upstream of the sample is compressed. As the air reaches a critical pressure, it forces the liquid sample plug to move forward through the microchannel. Pressure changes across the fluid sample as it moves through the channel are collected and stored on a PC equipped with an appropriate data acquisition

(DAQ) card. The flowing process of the sample is visualized, and the video is taken from above the manifold.

The viscosity is calculated via post-processing of the collected video and the pressure data after running the measurement. First, the video is analyzed to identify the time period over which the fluid sample is moving at a constant or near-constant velocity. This velocity is calculated using imaging software to track the dyed sample front as it moves through the channel by placing markers at equally spaced frames in the video. The uncertainty for this quantity is found using the standard deviation of the average velocity. It is needed for calculating the volumetric flow rate of the sample, as shown below:

$$Q = HW\bar{v}$$

where \bar{v} is the average velocity of the sample in the microchannel under a (quasi-)equilibrium condition.

During each time step, the dynamic contact angle and sample length are also measured using the imaging software. Average values of these three parameters are used in the above equations for calculating the shear stress, shear rate, volumetric flow rate and capillary pressure difference.

This microfluidic viscometer can be used to measure the viscosities of both Newtonian and non-Newtonian liquids without any procedural modifications. To that end, the viscosity of different wt% of glycerol in water solutions are measured and compared to the measurements of a commercially available cone/plate rheometer (Model: LVDV-III+; Brookfield Engineering Laboratories Inc, Middleboro, MA, USA) to validate the efficacy of the proposed invention. Furthermore, a non-Newtonian commercial eyedrop solution is measured and compared to the commercial rheometer over a range of shear rates. Finally, the viscosities of tears from both healthy eyes and dry eyes are measured using this microfluidic viscometer. After each run, the microfluidic chip is flushed clean with DI water, placed on a hot plate set to 50°C, and left to dry.

5.5 Validation

Both Newtonian and non-Newtonian liquids were measured using this microfluidic viscometer, and where possible a commercial rheometer, to validate the performance of the device. First, the viscosity of four different glycerol solutions ranging from 10 wt% to 70 wt% was measured

($n=3$) and compared to a commercially available cone/plate rheometer (Fig. 13). Glycerol solution was chosen because it is Newtonian fluid – its viscosity is independent of the applied shear rate – so the viscosity measurements can be compared to the commercial rheometer irrespective of deviations in the shear rate. In general, there was a close following between the measured viscosity using the microfluidic viscometer and the commercial rheometer. The measured viscosities of the glycerol/water solutions using the commercial rheometer were 1.21 ± 0.01 mPa·s, 2.19 ± 0.01 mPa·s, 5.02 ± 0.03 mPa·s, and 17.64 ± 0.14 mPa·s for the 10%, 30%, 50% and 70% solutions respectively. The percent difference between the averaged data points from the microfluidic viscometer and the commercial rheometer for the 10, 30, 50 and 70 wt% glycerol solutions was 6.93%, 3.24%, 4.39% and 3.42%, respectively.

The tests were conducted at room temperature ($\sim 25^\circ\text{C}$), and the surface tension values necessary for calculating the capillary pressure for each of the glycerol solutions were found by interpolating the results in Takamura *et al.* [61]. They used the Wilhelmy plate method to find the surface tension of a of number glycerol/water solutions at various temperatures with various salt concentrations. For the glycerol/water solutions used in this study, the surface tension values for the 10%, 30%, 50% and 70% solutions are 71.7 mN/m, 70.3 mN/m, 68.8 mN/m and 67.4 mN/m respectively. Images of the glycerol sample plug taken one second apart are shown in Fig. 14 to illustrate the receding dynamic contact angles. Appendix B presents the experimental data of the glycerol tests for one chip.

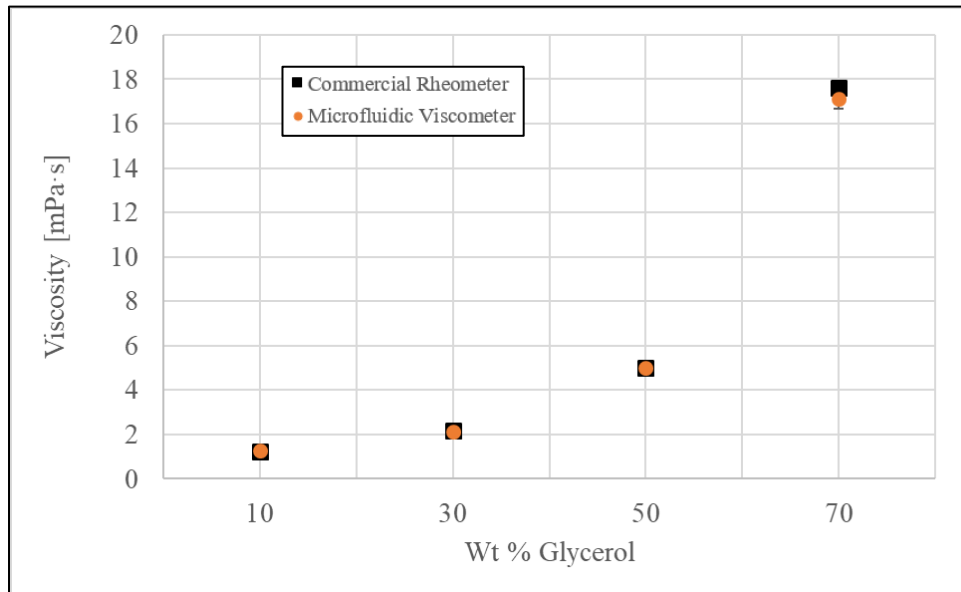


Figure 13. Viscosity of different weight percent glycerol in water solutions measured by the commercial rheometer (black) and the microfluidic viscometer (orange) ($n=3$)

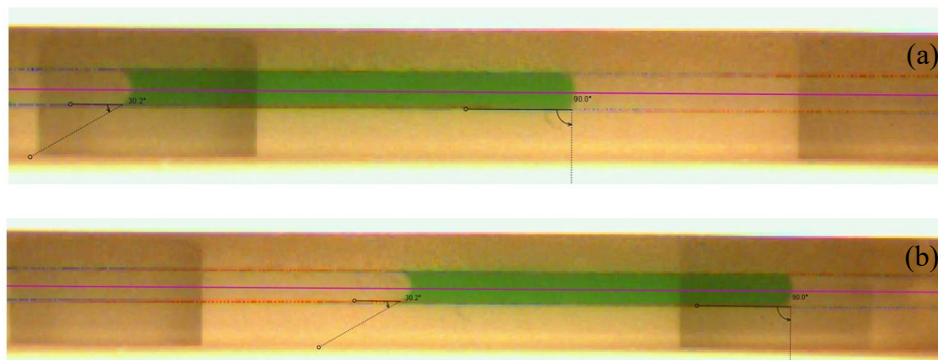


Figure 14. Glycerol plug moving through the microchannel from left to right at (a) $t = 20.8$ s, and (b) $t = 21.8$ s

Next, a non-Newtonian sample's shear viscosity was measured using both the Brookfield cone/plate rheometer and the microfluidic viscometer. A previous study was conducted to measure the viscosity of commercial eye drops (artificial tears) [4], and Systane Ultra High Performance (Alcon Laboratories, Inc.) was chosen to validate the microfluidic viscometer in this study. The surface tension value used when calculating the capillary pressure was 61.0 [62]. The viscosity of the

eye drop was measured using the commercial rheometer at shear rates between 24 – 316 s⁻¹ three times for each programmed pump flow rate. As expected, a shear thinning property was observed, with the viscosity decreasing with shear rate (Fig. 12).

For non-Newtonian fluids, the Weissenberg-Rabinowitsch-Mooney correction must be applied to the shear rate term [30]:

$$\dot{\gamma}_w = \frac{\dot{\gamma}_a}{3} \left[2 + \frac{d(\ln \dot{\gamma}_a)}{d(\ln \tau_w)} \right]$$

To compute the derivative term, it is common practice to plot $\ln(\dot{\gamma}_a)$ vs. $\ln(\tau_w)$ and use a second order polynomial to fit the data. The derivative term can then be found by taking the derivative of the best-fit quadratic (Fig. 15). For the artificial tear data, this derivative term is then:

$$\frac{d(\ln \dot{\gamma}_a)}{d(\ln \tau_w)} = 2(-0.01972) * \ln(\tau_w) + 1.3428$$

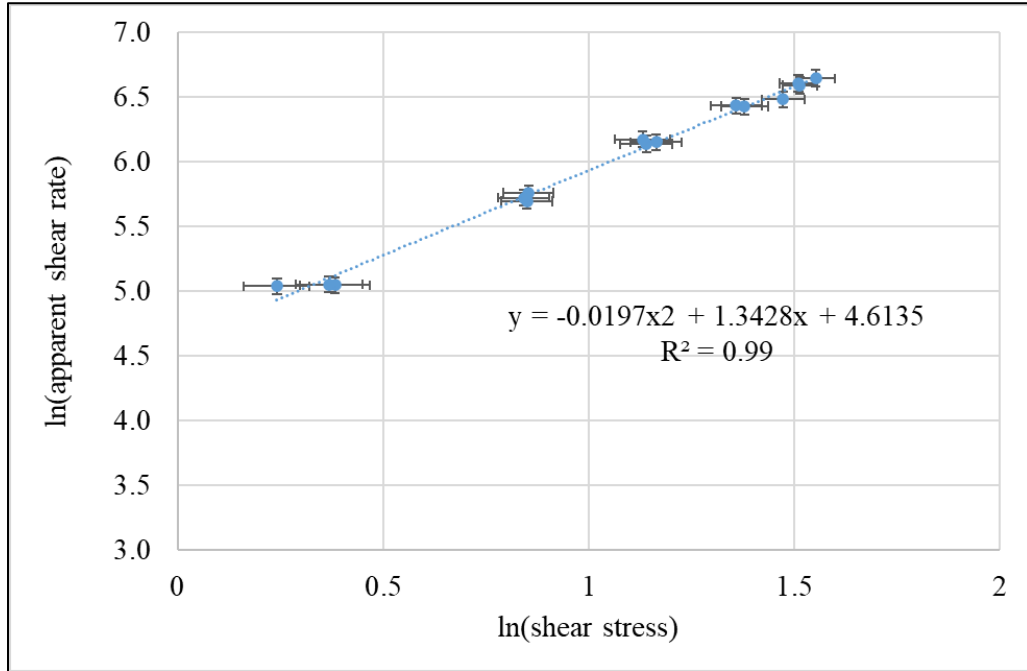


Figure 15. Plot of the natural logarithm of the shear stress versus the natural logarithm of shear rate for Systane Ultra High Performance (Alcon Laboratories, Inc.) eye drops

Thus, the true shear rate values can be found by plugging in the known shear stress values into the above derivative equation, which, along with the apparent shear rate, can be used to find the true shear rate value for each measurement. The error bars in Figure 16 are calculated using the propagated uncertainties for shear stress and apparent shear rate. For every data point τ_w with uncertainty u_{τ_w} , the uncertainty on $\ln(\tau_w)$ is $u_{\ln(\tau_w)} = \frac{u_{\tau_w}}{\tau_w}$. The same method is used to calculate the error bars for $\ln(\dot{\gamma}_a)$ in Fig. 16. Appendix C presents the experimental data for the non-Newtonian eyedrop.

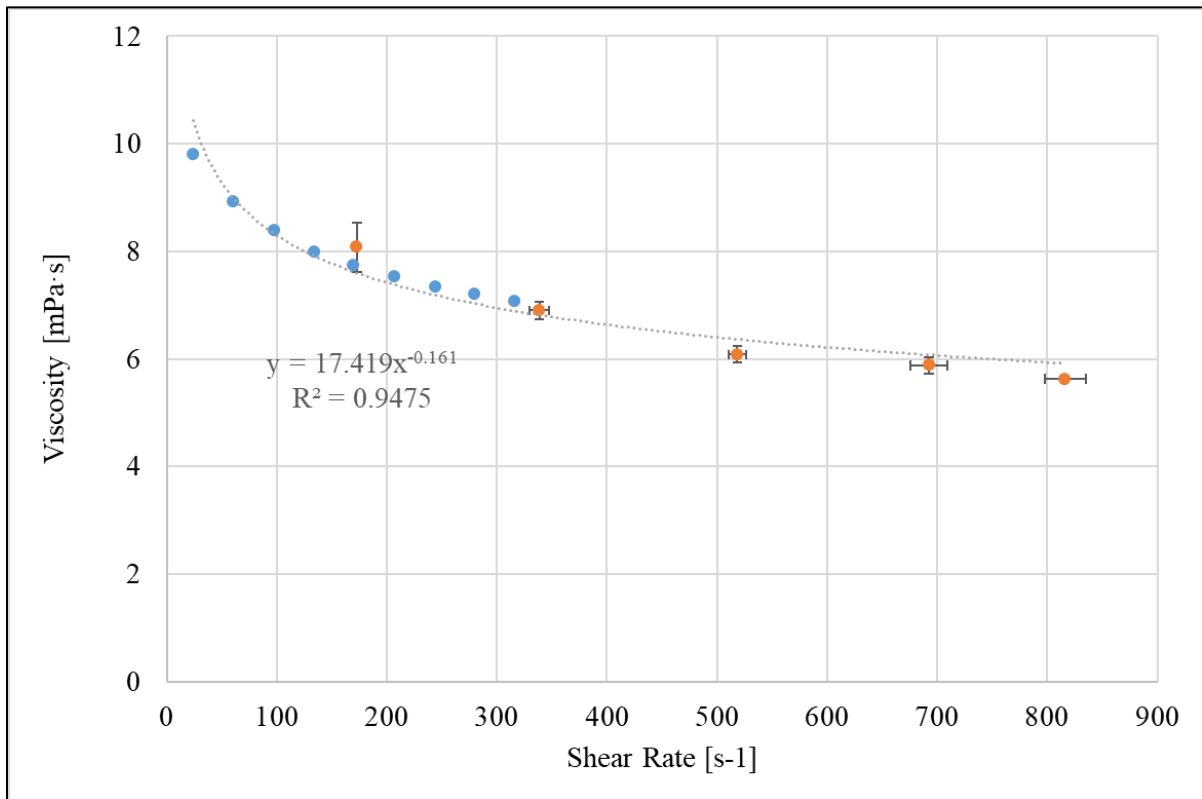


Figure 16. Systane Ultra High Performance (Alcon Laboratories, Inc.) eye drops measured using the commercial rheometer (blue) and the microfluidic viscometer (orange).

A power law formula was used to fit the data to quantify the shear-thinning property of the commercial eye drop. This is because the viscosity of commercial eye drops can be modelled using

the Ostwald-de Waele equation, derived from Newton’s Law of Viscosity [4]. For this particular eye drop, the flow consistency index $K(T)$ is $14.979 \text{ mPa}\cdot\text{s}^{0.871}$, and the flow behavior index is 0.871, indicating a shear-thinning fluid. Its equation relating shear rate to the shear viscosity is then: $\mu_{eff} = 14.979\dot{\gamma}^{-1.29}$. This mathematical model is necessary to determine the percent difference between the expected viscosity at a given shear rate and the measured viscosity using the microfluidic viscometer (Table 4).

Table 4 summarizes the key results from the experiment. When running a test using the microfluidic viscometer, the flow rate programmed into the syringe pump is used to vary the speed at which the sample moves through the microchannel, which informs the sample’s shear rate. For this study, five different pump flow rates were used (50, 100, 150, 200 and 250 $\mu\text{L}/\text{min}$), and their associated shear rates were calculated using the recorded video of the sample. These are listed in Table 1. The expected viscosity for the eye drop at the given shear rate is calculated by plugging the observed shear rate into the Ostwald-de Waele equation for the sample.

Table 4. Eye Drop Viscosity Validation

Pump Flow Rate [$\mu\text{L}/\text{min}$]	Shear Rate [s^{-1}]	Viscosity [$\text{mPa}\cdot\text{s}$]	Expected Viscosity [$\text{mPa}\cdot\text{s}$]	Viscosity Percent Difference [%]
50	173	8.48	7.71	9.60
	171	7.42	7.71	3.85
	174	8.32	7.70	7.70
100	350	6.71	7.04	4.74
	329	7.11	7.09	0.25
	337	6.89	7.07	2.60
150	509	6.14	6.70	8.82
	517	6.19	6.69	7.72
	529	5.86	6.67	12.91

200	683	5.70	6.45	12.45
	716	6.09	6.41	5.24
	679	5.85	6.46	9.94
250	842	5.61	6.28	11.39
	810	5.59	6.31	12.21
	798	5.69	6.33	10.53

Finally, samples of human tears were provided by the University of Waterloo’s Centre for Ocular Research & Education. The samples were taken from two separate volunteers – one that suffered from dry eye disease (DED) and one from a patient with healthy eyes. The viscosities were measured using the microfluidic viscometer at two different shear rates – one higher and one lower (Fig. 17). Due to the limited availability of the sample, two tests could be conducted at these two shear rates (n=3). The measured viscosity was found to be within the accepted range of human tears. Furthermore, the higher shear rate in both samples resulted in a lower viscosity, which illustrates the shear-thinning property of tear films.

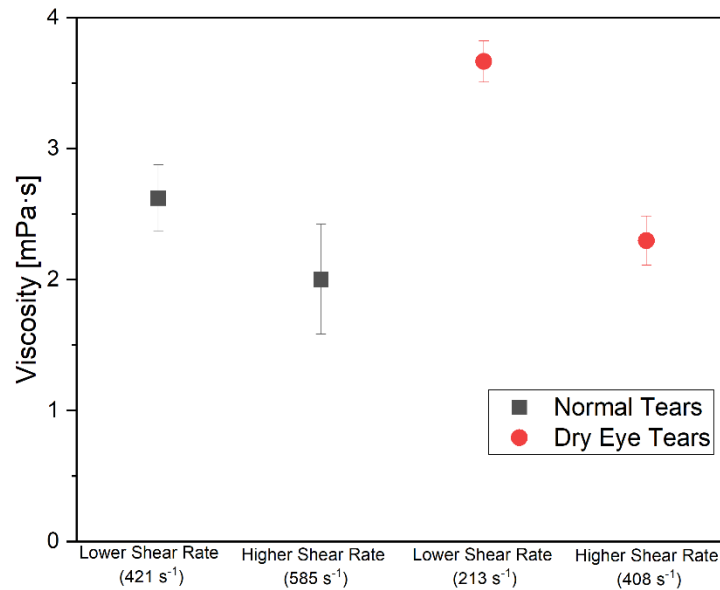


Figure 17. Viscosity of normal tears (grey) and dry eye tears (red) at two different shear rates

5.6 Discussion

The channel width was found by taking images of the channel at three separate locations along the channel at 4x zoom and using ImageJ to measure the width (3 times for each image). Averaging these nine measurements yielded a channel width of 1.46 ± 0.02 mm. After using a test solution of glycerol with known viscosity, the channel height was determined to be 0.134 ± 0.006 mm due to the presence of the surface coating. The pressure across the sample was measured with a differential pressure transducer with a total error band of 0.5% FS. Furthermore, to calculate capillary pressure, the receding dynamic contact angle is estimated to have an uncertainty of $\pm 5^\circ$, which is the resolution that is limited by the CMOS camera used. Finally, the uncertainty of the length measurement is estimated to be ± 0.4 mm, roughly the length of 4 pixels. The propagated relative uncertainty in a calculated value, $z(x,y,z,\dots)$, is given by the general formula:

$$\frac{\Delta z}{z} = \sqrt{\left(\frac{\partial f}{\partial w} \Delta w\right)^2 + \left(\frac{\partial f}{\partial x} \Delta x\right)^2 + \left(\frac{\partial f}{\partial y} \Delta y\right)^2 + \dots}$$

The relative uncertainty for the volumetric flow rate measurement is found by propagating the uncertainties of the velocity, channel height and channel width. This was calculated independently after each test.

$$\frac{\Delta Q}{Q} = \sqrt{\left(\frac{1}{v} \Delta v\right)^2 + \left(\frac{1}{H} \Delta H\right)^2 + \left(\frac{1}{W} \Delta W\right)^2}$$

It should be noted that since the velocity used to calculate the volumetric flow rate is found by taking the average velocities over the latter half of the test run, where the velocity is judged to be constant, indicating a quasi-equilibrium condition, the uncertainty in the velocity is given as its standard error:

$$\Delta v = \frac{\sigma_v}{\sqrt{N}}$$

This is similar to the way that the uncertainty in the measured differential pressure across the sample is calculated. Both the accuracy of the pressure transducer and the standard error of the averaged pressure values need to be taken into account. Because the measured differential pressure reached a steady value, its standard error was negligible compared to the uncertainty introduced by the accuracy of the pressure transducer. The errors due to pressure non-linearity, pressure hysteresis,

and thermal effect are included in this total error band for the pressure transducer. The uncertainty due to the resolution of the DAQ was negligible.

$$u_{\Delta P_{measured}} = \sqrt{\left(\frac{\sigma_{\Delta P}}{\sqrt{N}}\right)^2 + \left(\frac{0.5\% * FS}{100\%}\right)^2}$$

When calculating the capillary pressure, the uncertainty in the radius of curvature was found by taking half of the difference between the maximum and minimum radii of curvature. This value was found to be ± 0.002 mm. The uncertainty in the surface tension was found in literature. Finally, the total propagated uncertainty in the capillary pressure is given by the formula:

$$u_{P_{capillary}} = P_{capillary} \sqrt{\left(\frac{1}{\gamma} \Delta\gamma\right)^2 + \left(-\frac{1}{r} \Delta r\right)^2 + \left(\frac{1}{\cos\theta} \Delta\theta \sin\theta\right)^2}$$

The viscosity of a sample is found by dividing the sample's calculated shear stress by its calculated shear rate ($\mu = \frac{\tau_w}{\dot{\gamma}_w}$). The total relative uncertainty of the viscosity is then given by the equation:

$$\frac{\Delta\mu}{\mu} = \frac{\Delta\tau_w}{\tau_w} + \frac{\Delta\dot{\gamma}_w}{\dot{\gamma}_w}$$

Where the shear stress is given by: $\tau_w = \frac{WH(P_{meas} - P_{cap})}{2L_{sample}(W+H)}$.

The total uncertainty in the shear stress is then found by:

$$\Delta\tau_w = \sqrt{\left(\frac{\partial\tau_w}{\partial W} \Delta W\right)^2 + \left(\frac{\partial\tau_w}{\partial H} \Delta H\right)^2 + \left(\frac{\partial\tau_w}{\partial P_{meas}} \Delta P_{measured}\right)^2 + \left(\frac{\partial\tau_w}{\partial P_{capillary}} \Delta P_{capillary}\right)^2 + \left(\frac{\partial\tau_w}{\partial L_{sample}} \Delta L_{sample}\right)^2}$$

Similarly, for both Newtonian and non-Newtonian liquids, the shear rate is given by: $\dot{\gamma}_a = \frac{6Q}{WH^2}$. For, non-Newtonian liquids, however, an additional correction factor is required to obtain the true shear rate.

This means that the uncertainty in the shear rate was calculated using:

$$\Delta\dot{\gamma}_a = \sqrt{\left(\frac{\partial\dot{\gamma}_a}{\partial W} \Delta W\right)^2 + \left(\frac{\partial\dot{\gamma}_a}{\partial H} \Delta H\right)^2 + \left(\frac{\partial\dot{\gamma}_a}{\partial Q} \Delta Q\right)^2}$$

The measured viscosities and their associated uncertainties are given in Table 5. The largest sources of uncertainty are the measured pressure and the capillary pressure calculations. By improving the accuracy of the pressure transducer used, as well as using a higher resolution camera, these can be reduced. Furthermore, the volume of air in the tubing and fittings connected to the differential pressure transducer is negligible compared to the volume of air in the syringe and the chip used to propel the sample. Future work to optimize the loading channel of the microfluidic chip to reduce the sample size will be considered.

Table 5. Measurement Uncertainties Using Microfluidic Viscometer

Sample	Trial Number	Viscosity [mPa·s]	Propagated Uncertainty [± mPa·s]
10 wt% Glycerol	1	1.29	± 0.33
	2	1.27	± 0.27
	3	1.34	± 0.31
30 wt% Glycerol	1	2.02	± 0.41
	2	2.21	± 0.44
	3	2.15	± 0.48
50 wt% Glycerol	1	4.96	± 0.69
	2	4.72	± 0.64
	3	5.32	± 0.77
70 wt% Glycerol	1	16.94	± 1.85
	2	17.77	± 1.96
	3	16.70	± 1.83
50 µL/min Flow Rate Eye Drop	1	8.48	± 1.02
	2	7.42	± 0.85
	3	8.32	± 0.96

100 $\mu\text{L}/\text{min}$ Flow Rate Eye Drop	1	6.71	± 0.65
	2	7.11	± 0.70
	3	6.89	± 0.68
150 $\mu\text{L}/\text{min}$ Flow Rate Eye Drop	1	6.14	± 0.63
	2	6.19	± 0.61
	3	5.86	± 0.62
200 $\mu\text{L}/\text{min}$ Flow Rate Eye Drop	1	5.70	± 0.56
	2	6.09	± 0.54
	3	5.85	± 0.54
250 $\mu\text{L}/\text{min}$ Flow Rate Eye Drop	1	5.61	± 0.51
	2	5.59	± 0.49
	3	5.69	± 0.46

It should be noted that the accuracy of the Brookfield rheometer used for validation purposes has an accuracy of $\pm 1\%$ of the full-scale spindle/speed viscosity range. For the rheometer and spindle combination used to measure the viscosity of both the glycerol/water solutions and the Systane Ultra High Performance (Alcon Laboratories, Inc.) artificial tears, the full-scale viscosity range is found using the formula:

$$\text{Full - Scale Viscosity Range [mPa} \cdot \text{s]} = TK * SMC * \frac{10000}{RPM}$$

Where TK is the torque constant (which is 0.09373 for the LVDV-III+ rheometer model used), SMC is the spindle multiplier constant (which is 0.327 for the CP40 spindle used), and RPM is the programmed speed of the spindle (which was varied from 3.2 to 42.2 RPM for the artificial tear solution). This means that the viscosity measurements were accurate to $\pm 9.77\%$ at the lowest RPM setting, corresponding to a shear rate of 24 s^{-1} . At the highest RPM setting (shear rate of 316 s^{-1}), the viscosity measurements were accurate to $\pm 1.03\%$.

Based on the viscosity data collected from Tiffany [17] and outlined in Table 1, the proposed microfluidic viscometer's maximum measurement uncertainty of $\pm 12.0\%$ would be sufficient to compare the viscosities of healthy and dry eye tears. Additional testing of non-Newtonian liquids with different chips at lower flow rates would be needed to confirm the repeatability of low-shear viscosity measurements. To produce a measurement uncertainty of the proposed microfluidic viscometer that more in line with commercial rheometers at high shear rates, various adjustments to the system can be made, as outlined in Table 6. These include using a higher resolution camera to improve the uncertainty in the measured sample length, using a more sensitive differential pressure transducer, and improving the method by which the surface coating is applied to the channel to reduce irregularities further. Ultimately, there exists a trade-off between the overall cost of the system and marginal improvements in its accuracy.

Table 6. Systematic and Operational Uncertainty Analysis

Type of Error	Equipment	Property	Cost	Comments
Systematic	Camera + lens	5 MP Sensor: 2/3"	\$1378	In addition, increasing the resolution to 9 MP (Basler Ace acA4096-30uc USB 3.0 Color Camera, \$1740) with a 1" sensor and lens (12mm Focal Length, HP Series Fixed Focal Length Lens, \$810) with the correct orientation can reduce the total measurement uncertainty by 2.67%
	Pump	Cyclic	\$3500	For unidirectional measurement, does not affect measurement
		Accuracy (1.28 pL/min)		Flow rate uncertainty is negligible compared to programmed flow rate ($10^1 - 10^2 \mu\text{L}/\text{min}$)
	Transducer	$\pm 0.5\%$ FSS	\$123	The 10 in H ₂ O transducer, HV210-SM02-R (Superior Sensor Technology, Inc., Los Gatos, CA, \$79), has a total error band accuracy of $\pm 0.15\%$ FSS and can reduce the total measurement uncertainty by 0.65%
	Channel irregularity caused by surface coating	$\pm 1.4\%$	N/A	The surface coating reduced channel irregularities caused by laser cutting but did not eliminate them. A hypothetically perfectly smooth channel can reduce the total measurement uncertainty by 2.37%
	DAQ	$\pm 76 \mu\text{V}$	\$1400	Negligible uncertainty associated with voltage measurements ($\sim 0.02\%$)
	Light Source (heat)	2 x 40 W	N/A	No measurable increase in on-chip temperature
Operational	Chip (repeatability)	N/A	N/A	Further study required to determine

Chapter 6

Further Validation and Testing

6.1 Saliva

It is possible that this microfluidic viscometer can be used as a platform technology for measuring the viscosity of other biofluids. One such readily available water-based biofluid is human saliva. Saliva is made up of water, lipids, electrolytes, buffers and antimicrobial agents [63]. It acts as the initial defense against bacteria, hydrates mucous membranes and teeth, and aids in digestion, taste and deglutition [63]. Like tear films, human saliva contains a small percentage of lipids, but irregularities in the lipid concentration can be correlated to medical complications like dental caries [63].

Dental caries is the most ubiquitous dental disease [64]. It involves several factors, including susceptible teeth, dental plaque, consumption of carbohydrates, oral hygiene and salivary composition [64]. It was found that along with salivary pH and flow rate, salivary viscosity can be an indicator of dental caries [64]. One study found that the mean salivary viscosity of a group with caries was significantly higher than a caries-free group [64]. Another study found that a group with dental caries had frothy/bubbly saliva compared to a control group, suggesting increased viscosity [65]. It was noted that this increase in viscosity might be a result of reduced water content in the saliva [65]. The viscosity of saliva can therefore be a potential diagnostic tool orthodontists use to determine their patient's susceptibility to developing dental caries. Furthermore, because of its high-water content, it may be suitable for use with the existing hydrophobic channel coating.

Pooled human saliva was dyed with 10 v/v% green dye and measured using the Brookfield cone/plate rheometer (Model: LVDV-III+, Brookfield Engineering Laboratories Inc, MA, USA) and then measured using the microfluidic viscometer. Using the cone/plate rheometer, the viscosity was measured over the range of allowable shear rates. The viscosity using the microfluidic viscometer was measured using the syringe pump flow rate presets: 200 $\mu\text{L}/\text{min}$, 150 $\mu\text{L}/\text{min}$, 100 $\mu\text{L}/\text{min}$, and 50 $\mu\text{L}/\text{min}$ (Fig.18a) with $n=3$. All tests were conducted at room temperature ($\sim 24^\circ\text{C}$). The results show that the microfluidic viscometer has the potential to extend the shear rates to smaller values than what was capable with the Brookfield cone/plate rheometer. Furthermore, the microfluidic viscometer showed higher viscosities at these lower shear rates. When compared with literature [66], Fig. 18b

shows that for this range of shear rates, the viscosity should follow an upward trend with decreasing shear rates.

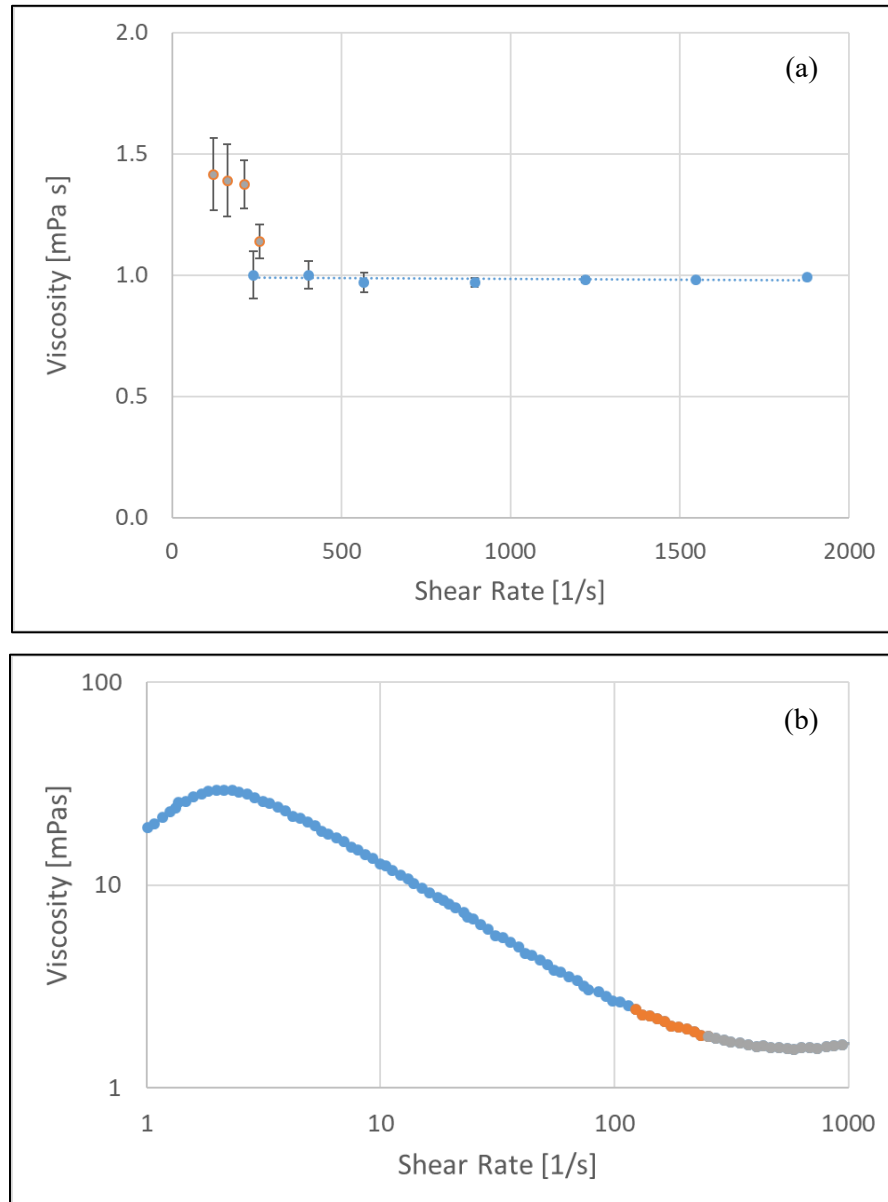


Figure 18. The shear viscosity of human tears: (a) measured using Brookfield cone/plate rheometer (blue) and microfluidic viscometer (orange); and (b) shear viscosity taken from Gittings *et al.* with the orange section of the curve at measured at the same shear rates as the microfluidic viscometer and

the grey section of curve measured at same shear rates as measured with the Brookfield cone/plate rheometer

6.2 Blood

The rheological properties of human blood depend on an assortment of factors, including shear rate, temperature, plasma viscosity, red blood cell viscosity, red blood cell membrane properties and red blood cell aggregation [67]. According to Chen *et al.*, alterations in blood viscosity are usually associated with issues with the natural function of endothelial cells and variations in shear stress from blood circulation, which has the potential to harm the circulatory system and associated organs [68]. Elevated cholesterol and triglyceride levels are related to increased viscosity in a patient's blood [68]. In addition, obesity, aging, and high sodium consumption have been also shown to increase blood viscosity [68]. Whole blood viscosity has been shown to be a significant factor for a host of illnesses, including hypertensive cardiac hypertrophy and coronary artery disease [69]. In addition, atypical blood viscosity plays a role in the progression of “cardio-cerebrovascular disease, hemorrhagic shock, renal disease, and diabetes” [68]. Furthermore, blood viscosity is a significant factor in drug evaluation and understanding their biochemical interactions [68].

A microfluidic viscometer capable of measuring whole blood viscosity is, therefore, a useful diagnostic tool for various diseases. Whole blood is a non-Newtonian, shear-thinning liquid [70]. The viscosity of whole porcine blood with Na citrate (Innovative Research, Inc., Novi, MI) was attempted to be measured using the microfluidic viscometer; however, a new cleaning protocol needed to be established as flushing the microchannel with water was not sufficient to remove all the blood residue. Therefore, a series of acrylic squares were treated with Aquapel, and their contact angle was measured to ensure successful treatment. Three water droplets were measured on each acrylic square, and the contact angle was processed using ImageJ. It was found that the Aquapel coating rendered the acrylic slide slightly hydrophobic. 5%, 1% and 0.5% H₂O₂ were added to the surface-treated acrylic squares, and new contact angle measurements were taken to determine if the hydrogen peroxide stripped away the coating. The results showed that only the treated acrylic with 0.5% H₂O₂ solution retained its hydrophobicity. As a final test, a section of Aquapel treated channel was imaged under a microscope before and after flushing it with 0.5% H₂O₂, and it was found that there was no noticeable change to the channel width (Fig 19).

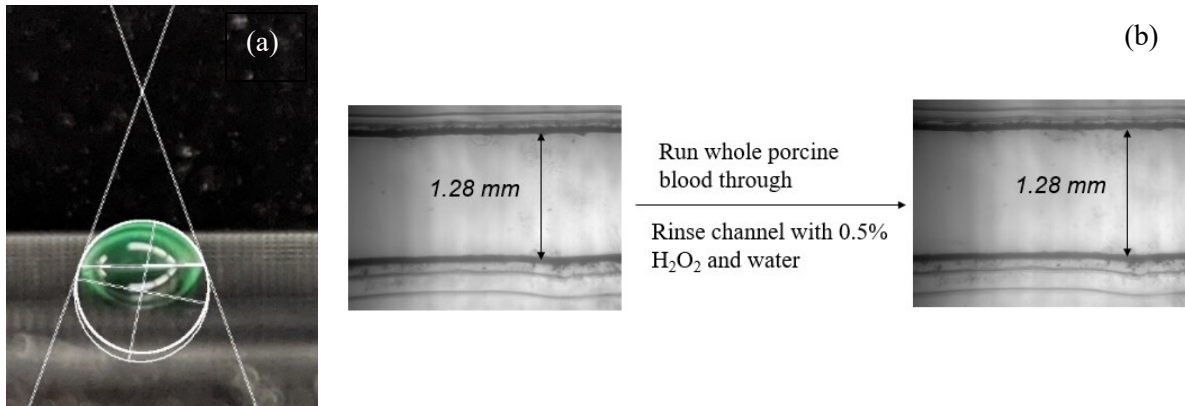


Figure 19. Hydrogen peroxide treatment validation: (a) contact angle test processed using ImageJ; and (b) section of microchannel before and after flowing porcine blood through and treating it with 0.5% H_2O_2 and water.

The viscosity of porcine whole blood was then tested at ambient temperature using a pump volumetric flow rate of $200 \mu\text{L}/\text{min}$, which was found to be roughly correlated to a shear rate of 317 s^{-1} . Because of the sample's deep reddish color, it did not need to be dyed. Furthermore, when calculating the capillary pressure contribution, the surface tension value used was $50.47 \text{ mN}/\text{m}$ [67]. This measured viscosity was compared to a theoretical viscosity model for porcine whole blood reported in literature. It was found that the measured viscosity had a high degree of repeatability between the three trials but was significantly higher than expected (Fig. 20). This discrepancy may be a result of the coating used on the microchannel. It is possible that the Aquapel may not be sufficiently repelling the blood, leading to a large amount of drag. This can lead to an over-estimation of the shear stress. Therefore, future tests involving blood would require an investigation into alternative channel coatings that are both compatible with acrylic and hydrogen peroxide.

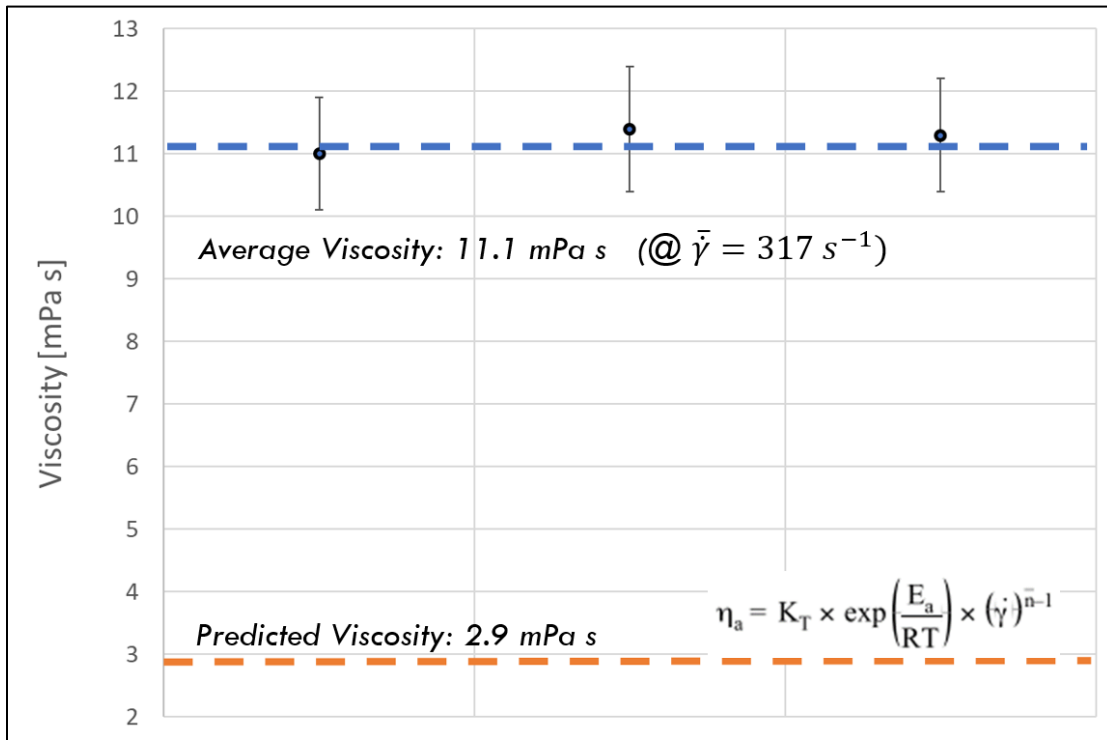


Figure 20. Viscosity of porcine whole blood measured using microfluidic viscometer (black circles), average viscosity measured using the microfluidic viscometer (blue line), and expected viscosity based on Rosentrater *et al.* [67] (orange line)

Chapter 7

Summary

A microfluidic viscometer with a programmable shear rate was built and validated using Newtonian (glycerol) and non-Newtonian liquids (artificial tears, saliva). First, the rheological properties of artificial tears were investigated to understand the dependence on temperature and shear rate. This understanding led to the development of mathematical models based on the Ostwald de Wale relationship to validate the microfluidic viscometer when the measured shear rate was out of the range of the cone/plate commercial rheometer.

Secondly, the different components of the microfluidic viscometer were either surveyed or built and iteratively improved until there was substantial agreement between the microfluidic viscometer and the cone/plate rheometer with Newtonian fluids. This involved investigating the noising forces (adhesion/channel roughness and interfacial tension) that led to overestimating the viscosity and finding ways to minimize them. This was done using a repellent channel coating, calculating the capillary pressure, and subtracting it from the total measured pressure drop across the sample. Finally, once the microfluidic viscometer was developed, it was validated using artificial tears.

Chapter 8

Future Recommendations

The following is a list of possible future steps to improve the microfluidic viscometer in terms of cost, accuracy, speed of processing and compatibility with a wide range of samples:

- To improve the accuracy of the microfluidic viscometer, a more sensitive differential pressure transducer can be used. In addition, a video camera with a higher resolution and pixel size can be used to capture a clearer image of the air-liquid interface. This will allow for better measurement of the sample length and the dynamic contact angle, reducing the overall uncertainty in the capillary pressure value.
- An investigation into the relationship between the channel geometry, pump volumetric flow rate and sample shear rate would be more practical than calculating the shear rate after a test has been performed.
- A more comprehensive range of biological samples should be tested along with compatible channel coatings.
- Automating the image analysis would reduce the run time of each experiment considerably.

To lower the overall cost of the system, replace the optical setup (lens + manifold with viewing slit) with a lens-less imaging solution. This will reduce spatial footprint and cost with a sufficient imaging capability.

References

- [1] U. Benelli, “Systane® lubricant eye drops in the management of ocular dryness,” *Clin. Ophthalmol.*, vol. 5, no. 1, pp. 783–790, 2011.
- [2] N. Yokoi, A. J. Bron, J. M. Tiffany, K. Maruyama, A. Komuro, and S. Kinoshita, “Relationship between tear volume and tear meniscus curvature,” *Arch. Ophthalmol.*, vol. 122, no. 9, pp. 1265–1269, 2004.
- [3] J. L. Gayton, “Etiology, prevalence, and treatment of dry eye disease,” *Clin. Ophthalmol.*, vol. 3, no. 1, pp. 405–412, 2009.
- [4] W. Kapadia *et al.*, “Shear-Thinning and Temperature-Dependent Viscosity Relationships of Contemporary Ocular Lubricants,” *Transl. Vis. Sci. Technol.*, vol. 11, no. 3, p. 1, Mar. 2022, doi: 10.1167/tvst.11.3.1.
- [5] J. P. Craig *et al.*, “TFOS DEWS II Report Executive Summary,” *Ocul. Surf.*, vol. 15, no. 4, pp. 802–812, Oct. 2017, doi: 10.1016/j.jtos.2017.08.003.
- [6] M. Uchino *et al.*, “Prevalence of Dry Eye Disease and its Risk Factors in Visual Display Terminal Users: The Osaka Study,” *Am. J. Ophthalmol.*, vol. 156, no. 4, pp. 759–766.e1, 2013, doi: 10.1016/j.ajo.2013.05.040.
- [7] M. T. Christensen *et al.*, “Clinical evaluation of an HP-guar gellable lubricant eye drop for the relief of dryness of the eye,” *Curr. Eye Res.*, vol. 28, no. 1, pp. 55–62, 2004.
- [8] R. Mencucci, C. Boccalini, R. Caputo, and E. Favuzza, “Effect of a hyaluronic acid and carboxymethylcellulose ophthalmic solution on ocular comfort and tear-film instability after cataract surgery,” *J. Cataract Refract. Surg.*, vol. 41, no. 8, pp. 1699–1704, 2015.
- [9] M. Baiula and S. Spampinato, “Experimental Pharmacotherapy for Dry Eye Disease: A Review,” *J. Exp. Pharmacol.*, vol. 13, pp. 345–358, 2021.
- [10] A. J. Bron *et al.*, “TFOS DEWS II pathophysiology report,” *Ocul. Surf.*, vol. 15, no. 3, pp. 438–510, 2017.
- [11] S. Adyanthaya and B. Abhilash, “Dry eye disease - are we underselling it? An epidemic in the offing and future management trends,” *Int. J. Med. Ophthalmology*, vol. 3, no. 1, pp. 41–43, 2021.
- [12] M. Uchino and D. A. Schaumberg, “Dry Eye Disease: Impact on Quality of Life and Vision,” *Curr. Ophthalmol. Rep.*, vol. 1, no. 2, pp. 51–57, Jun. 2013, doi: 10.1007/s40135-013-0009-1.
- [13] M. S. Milner *et al.*, “Dysfunctional tear syndrome: dry eye disease and associated tear film disorders – new strategies for diagnosis and treatment,” *Curr. Opin. Ophthalmol.*, vol. 28, no. SUPPLEMENT 1, pp. 3–47, Jan. 2017, doi: 10.1097/01.icu.0000512373.81749.b7.
- [14] J. P. Craig *et al.*, “TFOS DEWS II Definition and Classification Report,” *Ocul. Surf.*, vol. 15, no. 3, pp. 276–283, 2017.
- [15] Q. Findlay and K. Reid, “Dry eye disease: when to treat and when to refer,” *Aust. Prescr.*, vol. 41, no. 5, pp. 160–163, Oct. 2018, doi: 10.18773/austprescr.2018.048.
- [16] T. F. Svitova and M. C. Lin, “Dynamic interfacial properties of human tear-lipid films and their interactions with model-tear proteins in vitro,” *Adv. Colloid Interface Sci.*, vol. 233, pp. 4–24, Jul. 2016, doi: 10.1016/j.cis.2015.12.009.
- [17] J. M. Tiffany, “The viscosity of human tears,” *Int. Ophthalmol.*, vol. 15, pp. 371–376, 1991.
- [18] L. E. Downie, J. Lee, E. Makrai, A. McDonnell, and L. Yeo, “A novel approach to identifying dry eye disease using acoustically-driven microfluidic extensional rheometry,” *Invest. Ophthalmol. Vis. Sci.*, vol. 60, no. 9, pp. 4189–4189, Jul. 2019.

- [19] W. Scherz, M. G. Doane, and C. H. Dohlman, "Tear volume in normal eyes and keratoconjunctivitis sicca," *Albrecht Von Graefes Arch. Für Klin. Exp. Ophthalmol.*, vol. 192, no. 2, pp. 141–150, 1974, doi: 10.1007/BF00410700.
- [20] R. J. Marshall, "Milk," in *Encyclopedia of Food Sciences and Nutrition*, Second Edi., 2003, pp. 3963–3968. doi: 10.1016/b0-12-227055-x/01121-4.
- [21] G. Schramm, *A Practical Approach to Rheology and Rheometry*, 2nd ed. ThermoHaake Rheology.
- [22] E. V. Gonçalves and S. C. da S. Lannes, "Chocolate rheology," *Ciênc. E Tecnol. Aliment.*, vol. 30, no. 4, pp. 845–851, Dec. 2010, doi: 10.1590/S0101-20612010000400002.
- [23] R. Islam, M. Rahman, S. Ahmed, and M. R. Halder, "A Coaxial Cylinder Type Rotational Viscometer- Design and Optimization," *Int. J. Sci. Eng. Res.*, vol. 7, no. 10, pp. 1792–1796, 2016.
- [24] Raymond. McKennell, "Cone-Plate Viscometer Comparison with Coaxial Cylinder Viscometer," *Anal. Chem.*, vol. 28, no. 11, pp. 1710–1714, Nov. 1956, doi: 10.1021/ac60119a021.
- [25] L. Shang, Y. Cheng, and Y. Zhao, "Emerging Droplet Microfluidics," *Chem. Rev.*, vol. 117, no. 12, pp. 7964–8040, 2017.
- [26] L. Xu, A. Wang, X. Li, and K. W. Oh, "Passive micropumping in microfluidics for point-of-care testing," *Biomicrofluidics*, vol. 14, no. 3, 2020.
- [27] R. Z. Gao, M. Hébert, J. Huissoon, and C. L. Ren, "µPump: An open-source pressure pump for precision fluid handling in microfluidics," *HardwareX*, vol. 7, 2020.
- [28] S. Solanki, C. M. Pandey, R. K. Gupta, and B. D. Malhotra, "Emerging Trends in Microfluidics Based Devices," *Biotechnol. J.*, vol. 15, no. 5, p. 1900279, May 2020, doi: 10.1002/biot.201900279.
- [29] G. M. Whitesides, "The origins and the future of microfluidics," *Nature*, vol. 442, no. 7101, pp. 368–373, Jul. 2006, doi: 10.1038/nature05058.
- [30] C. J. Pipe, T. S. Majmudar, and G. H. McKinley, "High shear rate viscometry," *Rheol. Acta*, vol. 47, no. 5–6, pp. 621–642, Jul. 2008, doi: 10.1007/s00397-008-0268-1.
- [31] J. Chevalier and F. Ayela, "Microfluidic on chip viscometers," *Rev. Sci. Instrum.*, vol. 79, no. 7, p. 076102, Jul. 2008, doi: 10.1063/1.2940219.
- [32] S. Gupta, W. S. Wang, and S. A. Vanapalli, "Microfluidic viscometers for shear rheology of complex fluids and biofluids," *Biomicrofluidics*, vol. 10, no. 4, p. 043402, Jul. 2016.
- [33] A. McDonnell, J. Lee, E. Makrai, L. Y. Yeo, and L. E. Downie, "Tear Film Extensional Viscosity Is a Novel Potential Biomarker of Dry Eye Disease," *Ophthalmology*, vol. 126, no. 8, pp. 1196–1198, Aug. 2019, doi: 10.1016/j.ophtha.2019.03.014.
- [34] E. Macosko and M. Goldman, *Drop-Seq Laboratory Protocol version 1.1*. Steve McCarroll's Lab, Harvard Medical School, 2015.
- [35] L. Jones *et al.*, "TFOS DEWS II Management and Therapy Report," *Ocul. Surf.*, vol. 15, no. 3, pp. 575–628, 2017.
- [36] R. Rangarajan, B. Kraybill, A. Ogundele, and H. A. Ketelson, "Effects of a hyaluronic acid/hydroxypropyl guar artificial tear solution on protection, recovery, and lubricity in models of corneal epithelium," *J. Ocul. Pharmacol. Ther.*, vol. 31, no. 8, pp. 491–497, 2015.
- [37] P. Simmons and J. Vehige, "Investigating the potential benefits of a new artificial tear formulation combining two polymers," *Clin. Ophthalmol.*, vol. Volume 11, pp. 1637–1642, Sep. 2017, doi: 10.2147/OPHTH.S135550.
- [38] A. Pucker, M. Marrone, and J. J. Nichols, "Over the counter (OTC) artificial tear drops for dry eye syndrome," *Cochrane Database Syst. Rev.*, vol. CD009729, no. 2, 2012.

- [39] S. Barabino *et al.*, “Dry eye disease treatment: The role of tear substitutes, their future, and an updated classification,” *Eur. Rev. Med. Pharmacol. Sci.*, vol. 24, no. 17, pp. 8642–8652, 2020.
- [40] P. Daull *et al.*, “Cationic Emulsion-Based Artificial Tears as a Mimic of Functional Healthy Tear Film for Restoration of Ocular Surface Homeostasis in Dry Eye Disease,” *J. Ocul. Pharmacol. Ther.*, vol. 36, no. 6, pp. 355–365, 2020.
- [41] R. Garofalo, C. Kunnen, R. Rangarajan, V. Manoj, and H. Ketelson, “Relieving the symptoms of dry eye disease: update on lubricating eye drops containing hydroxypropyl-guar,” *Clin. Exp. Optom.*, vol. 104, no. 8, pp. 826–834, 2021.
- [42] S. Srinivasan and V. Manoj, “A decade of effective dry eye disease management with systane ultra (Polyethylene glycol/propylene glycol with hydroxypropyl guar) lubricant eye drops,” *Clin. Ophthalmol.*, vol. 15, pp. 2421–2435, 2021.
- [43] Y. J. Yang, W. Y. Lee, Y. J. Kim, and Y. P. Hong, “A meta-analysis of the efficacy of hyaluronic acid eye drops for the treatment of dry eye syndrome,” *Int. J. Environ. Res. Public Health*, vol. 18, no. 5, pp. 1–14, 2021.
- [44] J. Q. Hall, W. H. Ridder, A. L. Nguyen, and J. R. Paugh, “Visual effect and residence time of artificial tears in dry eye subjects,” *Optom. Vis. Sci.*, vol. 88, no. 7, pp. 872–880, 2011.
- [45] A. Urtti, “Challenges and obstacles of ocular pharmacokinetics and drug delivery,” *Adv. Drug Deliv. Rev.*, vol. 58, no. 11, pp. 1131–1135, 2006.
- [46] H. Zhu and A. Chauhan, “Effect of viscosity on tear drainage and ocular residence time,” *Optom. Vis. Sci.*, vol. 85, no. 8, pp. 715–725, 2008.
- [47] S. Bandlitz, C. Purslow, P. J. Murphy, and H. Pult, “Time course of changes in tear meniscus radius and blink rate after instillation of artificial tears,” *Invest. Ophthalmol. Vis. Sci.*, vol. 55, no. 9, pp. 5842–5847, 2014.
- [48] J. Wang, J. Aquavella, J. Palakuru, and S. Chung, “Repeated measurements of dynamic tear distribution on the ocular surface after instillation of artificial tears,” *Invest. Ophthalmol. Vis. Sci.*, vol. 47, no. 8, pp. 3325–3329, 2006.
- [49] J. R. Palakuru, J. Wang, and J. V. Aquavella, “Effect of blinking on tear volume after instillation of mid-viscosity artificial tears,” *Am. J. Ophthalmol.*, vol. 146, no. 6, pp. 920–924, 2008.
- [50] F. A. Che Arif, M. R. Hilmi, K. Mohd Kamal, and M. H. Ithnin, “Evaluation of 18 artificial tears based on viscosity and pH,” *Malays. J. Ophthalmol.*, vol. 2, no. 2, pp. 96–111, 2020.
- [51] C. I. Tung *et al.*, “Noninvasive, objective, multimodal tear dynamics evaluation of 5 over-the-counter tear drops in a randomized controlled trial,” *Cornea*, vol. 31, no. 2, pp. 108–114, 2012.
- [52] C. J. Seeton, “Viscosity-temperature correlation for liquids,” *Tribol. Lett.*, vol. 22, no. 1, pp. 67–78, 2006.
- [53] A. M. Shah and A. Galor, “Impact of ocular surface temperature on tear characteristics: Current insights,” *Clin. Optom.*, vol. 13, pp. 51–62, 2021.
- [54] A. U. Oza and D. C. Venerus, “The dynamics of parallel-plate and cone-plate flows,” *Phys. Fluids*, vol. 33, no. 2, p. 023102, Feb. 2021, doi: 10.1063/5.0036980.
- [55] “Brookfield Digital Rheometer Model DV-III+ Manual No. M/98-211-A0701,” Brookfield Engineering Laboratories.
- [56] Malvern Instruments, “A Basic Introduction to Rheology,” *Whitepaper*. pp. 1–19, 2016.
- [57] J. R. Paugh, A. L. Nguyen, H. A. Ketelson, M. T. Christensen, and D. L. Meadows, “Precorneal residence time of artificial tears measured in dry eye subjects,” *Optom. Vis. Sci.*, vol. 85, no. 8, pp. 725–731, 2008.
- [58] S. Arshinoff, I. Hofmann, and H. Nae, “Rheological behavior of commercial artificial tear solutions,” *J. Cataract Refract. Surg.*, vol. 47, no. 5, pp. 649–654, 2021.

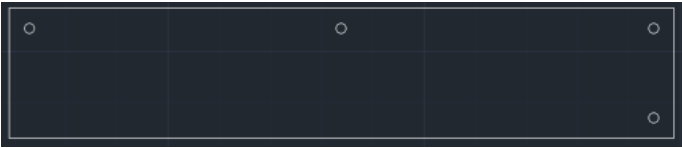
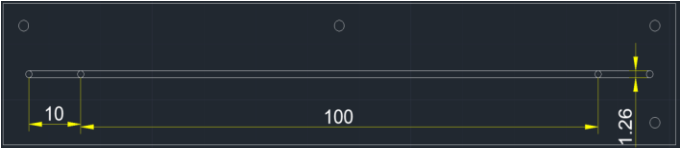
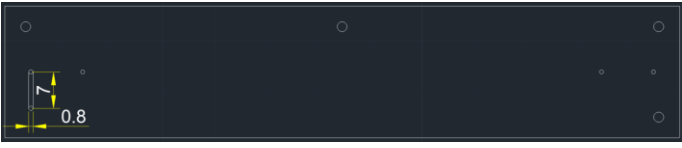
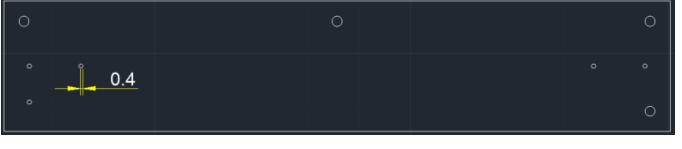
- [59] M. Q. Rahman, K. S. Chuah, E. C. A. MacDonald, J. P. M. Trusler, and K. Ramaesh, "The effect of pH, dilution, and temperature on the viscosity of ocular lubricants-shift in rheological parameters and potential clinical significance," *Eye Basingstoke*, vol. 26, no. 12, pp. 1579–1584, 2012.
- [60] T. Glawdel, C. Elbuken, and C. L. Ren, "Droplet formation in microfluidic T-junction generators operating in the transitional regime. I. Experimental observations," *Phys. Rev. E - Stat. Nonlinear Soft Matter Phys.*, vol. 85, no. 1, pp. 1–9, 2012.
- [61] K. Takamura, H. Fischer, and N. R. Morrow, "Physical properties of aqueous glycerol solutions," *J. Pet. Sci. Eng.*, vol. 98–99, pp. 50–60, Nov. 2012, doi: 10.1016/j.petrol.2012.09.003.
- [62] K. Han, O. E. Woghiren, and R. Priefer, "Surface tension examination of various liquid oral, nasal, and ophthalmic dosage forms," *Chem. Cent. J.*, vol. 10, no. 1, p. 31, Dec. 2016, doi: 10.1186/s13065-016-0176-x.
- [63] F. Fineide *et al.*, "Characterization of Lipids in Saliva, Tears and Minor Salivary Glands of Sjögren's Syndrome Patients Using an HPLC/MS-Based Approach," *Int. J. Mol. Sci.*, vol. 22, no. 16, p. 8997, Aug. 2021, doi: 10.3390/ijms22168997.
- [64] D. Animireddy, V. Reddy Bekkem, P. Vallala, S. Kotha, S. Ankireddy, and N. Mohammad, "Evaluation of pH, buffering capacity, viscosity and flow rate levels of saliva in caries-free, minimal caries and nursing caries children: An in vivo study," *Contemp. Clin. Dent.*, vol. 5, no. 3, p. 324, 2014, doi: 10.4103/0976-237X.137931.
- [65] V. K. Gopinath and A. R. Arzreanne, "Saliva as a Diagnostic Tool for Assessment of Dental Caries," *Arch. Orofac. Sci.*, vol. 1, pp. 57–59, 2006.
- [66] S. Gittings, N. Turnbull, B. Henry, C. J. Roberts, and P. Gershkovich, "Characterisation of human saliva as a platform for oral dissolution medium development," *Eur. J. Pharm. Biopharm.*, vol. 91, pp. 16–24, Apr. 2015, doi: 10.1016/j.ejpb.2015.01.007.
- [67] K. A. Rosentrater and R. A. Flores, "PHYSICAL AND RHEOLOGICAL PROPERTIES OF SLAUGHTERHOUSE SWINE BLOOD AND BLOOD COMPONENTS," *Trans. ASAE*, vol. 40, no. 3, pp. 683–689, 1997, doi: 10.13031/2013.21287.
- [68] G. Chen, L. Zhao, Y. Liu, F. Liao, D. Han, and H. Zhou, "Regulation of blood viscosity in disease prevention and treatment," *Chin. Sci. Bull.*, vol. 57, no. 16, pp. 1946–1952, 2012, doi: 10.1007/s11434-012-5165-4.
- [69] G. de Simone, R. B. Devereux, S. Chien, M. H. Alderman, S. A. Atlas, and J. H. Laragh, "Relation of Blood Viscosity to Demographic and Physiologic Variables and to Cardiovascular Risk Factors in Apparently Normal Adults," *Circulation*, vol. 81, no. 1, pp. 107–117, Jan. 1990.
- [70] A. V. Cardoso and A. O. Camargos, "Geometrical Aspects During Formation of Compact Aggregates of Red Blood Cells," *Mater. Res.*, vol. 5, no. 3, pp. 263–268, Sep. 2002, doi: 10.1590/S1516-14392002000300008.

Appendices

Appendix A

Chip Fabrication Procedure

1. Create AutoCAD Files for Each Layer





Layer	AutoCAD Design (lengths in mm)	Properties
Bottom “Layer 1”		Acrylic Thickness: ~1.6 mm
Main Channel “Layer 2”		Acrylic adhesive film Thickness: ~134 μm
Loading Channel “Layer 3”		Acrylic Thickness: ~1.6 mm Acrylic adhesive Thickness: 100 μm
Cover Film “Layer 4”		Polyester film Thickness: 100 μm

2. Pre-Laser Cutting

- Set AutoCAD design to red colored lines. Save designs as .dxf
- For all AutoCAD designs, remove ports within the channels before laser cutting
- Open with CorelDraw. Click “object” → “properties” → “no fill”, “line size: 0.001 in”.
“File” → “print” → select laser cutter and print
- Open UCP software. Change material/print settings accordingly.
- Tip: if duplicate images are not showing up use the “duplicate view” button on the main screen

- Ensure the orientation and spacing of the material on the laser cutting stage is reflected in the UCP software so as to not run the laser on the stage. Select the top-left pointer on the design and change the x&y position in the software accordingly

3. Laser Cutting

Description	Material	Printer Specs	Picture	Notes
Laser cut bottom layer	Acrylic Sheet	Thickness: 0.063” Speed: 10%		
Assemble and laser cut the loading channel layer	Acrylic Sheet + White 1” double-sided acrylic tape	Material: Acrylic Thickness: 0.065” Speed: 10%		Secure acrylic sheet to table before applying tape May need to flip the .dxf file horizontally in CorelDraw so the guide holes match with the bottom layer
Laser cut channel layer	Double-sided acrylic adhesive – Arcare 90106NB	Material: Acrylic Thickness: 0.01” Speed: 16%		Cut out a piece of material from the roll and tape down to laser cutting stage
Laser cut the cover layer	#8187K12 Polyester Film	Material: PET-G Thickness: 0.004” Speed: 22%		Yellow-colored residue after printing. Clean with kimwipe and IPA Clean laser cutting stage

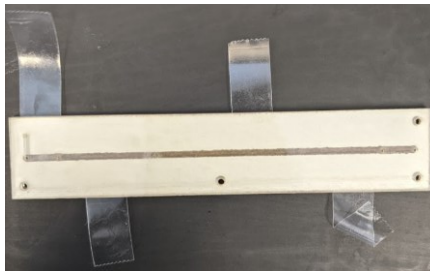
4. Assembly

- a. Remove adhesive back from **layer 3**. Rest it on guide pegs. Lower **layer 4** onto it and press inside to out. Use electrical tape roll to remove bubbles from ports



- b. Remove protective film from **layer 1**. Rest it on guide pegs. Apply double-sided tape to **layer 2** and lower it onto layer 1.
- a. The tape should go directly on to the adhesive covering of layer 2
 - b. Apply the tape far away from the channel

Remove the adhesive back of **layer 2** and the protective cover of **layer 3** (bottom). Lower **layer 3** onto **layer 2**.



- c. Separate **layer 1** and **layer 2** by hand (it's only held together by a few pieces of double-sided tape). Remove protective film and rest **layer 1** on guide pegs. Remove adhesive back and lower **layer 2** onto **layer 1**



Appendix B

Glycerol Experimental Data

	10 v/v% Glycerol			30 v/v% Glycerol			50 v/v% Glycerol			70 v/v% Glycerol		
P_{measured} [Pa]	1329.78	1412.73	1370.44	1413.5	1419.00	1364.10	1745.2	1719.65	1702.5	2633.18	2598.89	2559.85
Average Velocity [mm/s]	10.055	14.285	10.725	14.396	10.670	10.666	10.339	10.617	10.230	8.655	9.104	7.308
Q [mm ³ /s]	1.967	2.795	2.098	2.816	2.087	2.087	2.023	2.077	2.001	1.693	1.781	1.430
Surface Tension [mN/m]	71.726	71.726	71.726	70.279	70.279	70.279	68.832	68.832	68.832	67.385	67.385	67.385
Theta [°]	15.100	19.300	16.000	30.200	25.400	26.200	30.600	24.600	32.700	37.600	32.200	20.700
$P_{\text{capillary}}$ [Pa]	1128.444	1103.114	1123.522	989.783	1034.516	1027.556	965.439	1019.832	943.869	869.977	929.166	1027.169
Total Pressure [Pa]	201.342	309.617	246.918	423.717	384.493	336.548	779.812	699.827	758.642	1763.204	1669.724	1532.687
L_{sample} [mm]	25.333	25.610	25.787	21.752	24.368	21.940	22.749	20.898	20.798	17.993	15.443	18.792
Viscosity [mPa·s]	1.29	1.27	1.34	2.02	2.21	2.15	4.96	4.72	5.32	16.94	17.77	16.70

Appendix C

Systane Ultra High Performance Experimental Data

	50 $\mu\text{L}/\text{min}$			100 $\mu\text{L}/\text{min}$			150 $\mu\text{L}/\text{min}$			200 $\mu\text{L}/\text{min}$		
P_{measured} [Pa]	1446.931	1474.173	1471.704	1736.945	1725.286	1720.929	1829.678	1866.977	1769.086	1984.100	2036.602	2152.910
Average Velocity [mm/s]	3.481	3.447	3.499	7.088	6.655	6.820	10.349	10.503	10.736	13.907	14.607	13.833
Q [mm ³ /s]	0.681	0.674	0.685	1.387	1.302	1.334	2.025	2.055	2.100	2.721	2.858	2.706
Surface Tension [mN/m]	60.88	60.88	60.88	60.88	60.88	60.88	60.88	60.88	60.88	60.88	60.88	60.88
Theta [°]	18.9	18.1	18.7	23.6	26.1	24.7	38.6	40.6	39.5	32	32.7	33.1
$P_{\text{capillary}}$ [Pa]	938.568	942.963	939.684	909.081	890.892	901.289	775.310	753.238	765.493	841.309	834.824	831.062
Total Pressure [Pa]	508.363	531.210	532.020	827.864	834.394	819.640	1054.368	1113.739	1003.593	1142.791	1201.778	1321.848
L_{sample} [mm]	21.275	25.610	22.583	21.630	21.907	21.674	20.698	21.353	19.878	16.288	17.584	18.042
Viscosity [mPa·s]	8.48	7.42	8.32	6.71	7.11	6.89	6.14	6.19	5.86	5.70	6.09	5.85

Table Continued:

	250 $\mu\text{L}/\text{min}$		
P_{measured} [Pa]	2106.148	2170.439	2321.642
Average Velocity [mm/s]	17.183	16.523	16.276
Q [mm ³ /s]	3.362	3.233	3.184
Surface Tension [mN/m]	60.88	60.88	60.88
Theta [°]	20.800	23.100	24.200
$P_{\text{capillary}}$ [Pa]	927.398	912.513	904.872
Total Pressure [Pa]	1178.750	1257.926	1416.770
L_{sample} [mm]	15.333	17.062	19.146
Viscosity [mPa·s]	5.61	5.59	5.69